Environmental Science and Pollution Research (2022) 29:85413–85432
https://doi.org/10.1007/s11356-022-21754-1

RESEARCH ARTICLE

Effect of oxidative and non-oxidative conditions on molecular size fractionation of humic acids: TiO_2 and Cu-doped TiO_2 photocatalysis

Ceyda S. Uyguner-Demirel[1] · Nazli Turkten[2] · Dila Kaya[3] · Miray Bekbolet[1]

Received: 31 March 2022 / Accepted: 26 June 2022 / Published online: 6 July 2022

Abstract

Natural waters contain some carbonaceous materials referred to as dissolved organic matter, which is mainly composed of humic acids (HA). Owing to its polydispersed character related to the presence of diverse molecular size fractions (< 450 kDa to even < 1 kDa), HA displays curious reactivity in natural waters and during water treatment train. In this study, a system-based stepwise approach was tracked by characterizing HA following photolysis, adsorptive interactions, and solar photocatalysis using bare TiO_2, sol–gel prepared TiO_2, and their respective Cu-doped specimens complementary to kinetic evaluation on this respect. For this purpose, prior to and following each treatment, HA was monitored by dissolved organic carbon content, UV–vis parameters, and fluorescence features. Attenuated total reflection Fourier transform infrared (FTIR), surface-enhanced Raman scattering spectroscopy (SERS), XRD, SEM, EDAX XPS, and DRS were used to characterize the materials and solutions reported in this study. Most significant quantitative variations were attained in UV–vis spectroscopic parameters along with fluorescence characteristics; however, infrared and Raman profiles displayed slight deviations in qualitative measures. Differentiation between the selected photocatalyst specimens could be visualized through molecular size effects pointing out the significance of HA 10 kDa fraction. For the first time, this study reports the degradation of specific fractions of HA as a function of their molecular size fraction. Cu-TiO_2 seems to photocatalyze more effectively the degradation of the diverse HA fractions due to their more extended absorption of solar light by this photocatalyst.

Keywords Cu-doped TiO_2 · Humic acid · Molecular size fractions · UV–vis · Fluorescence · Infrared and Raman spectroscopy

Introduction

The amount, character, and properties of dissolved organic matter (DOM) vary according to the origin of water and depend on the biogeochemical cycles of their surrounding environment. As a carrier of metals and hydrophobic organic chemicals, DOM significantly affects potable water quality by contributing to undesirable aesthetic problems such as color, taste, and odor. Moreover, the seasonal variability of DOM concentration poses challenges to water treatment facilities. It has also been demonstrated that DOM related dissolved organic carbon (DOC) contents play a crucial role in climate change (Porcal et al. 2009; Navarro-Pedreño et al. 2021). DOM is a heterogeneous mixture of components varying in size and composition. Polydisperse nature of DOM has been considered as responsible for the preferential sorption of its certain fractions onto various oxide surfaces (Hur and Schlautman 2003). Within this context, understanding the characteristics of DOM and its fractions at various stages of treatment train would be substantially important.

Being the acid insoluble (pH < 2) fraction of DOM, humic acids (HAs) are defined as amorphous supramolecular macromolecules composed of multifunctional aromatic components linked by a variety of aliphatic moieties mainly composed of carboxylic and phenolic functional groups expressing redox properties (Hayes et al. 1989; Chi and

Responsible Editor: Sami Rtimi

✉ Ceyda S. Uyguner-Demirel
uygunerc@boun.edu.tr

[1] Institute of Environmental Sciences, Bogazici University, Bebek, Istanbul 34342, Turkey

[2] Department of Chemistry, Faculty of Arts and Sciences, Kirsehir Ahi Evran University, Kirsehir 40100, Turkey

[3] Department of Chemistry, Faculty of Engineering and Natural Sciences, Istanbul Medeniyet University, Istanbul 34700, Turkey

Amy 2004; Tian et al. 2018; Capasso et al. 2020). Due to the presence of dense aromatic and aliphatic skeleton with various regions of conjugated systems, hetero atoms, and functional groups, HAs display spectroscopic features under all environmental conditions as well as through all steps of treatment train (Chen et al. 2002; Uyguner and Bekbolet 2005, 2009; Brezinski and Gorczyca 2019; Chen and Yu 2021; Thomson et al. 2004). The polydispersity properties of humic matter resulted in a definition expressing HA as devoid of a constant polymeric structure (Chin et al. 1994; Tanaka 2012). Due to these complex properties, molecular size fractions of HA could express diverse behavior under natural water environments as well as differing reactivities towards both photolytic and photocatalytic conditions.

Employment of TiO_2-based nanomaterials as photocatalyst specimens has attracted prodigious interest in various fields of applications since decades (Noman et al. 2019; Gowland et al. 2021; Zhang et al. 2021). However, the major disadvantage related to band-gap energy limiting the use of UVA light sources also attracted widespread consideration. Among a variety of metal ions (e.g., Mn^{2+}, Fe^{3+}, Cr^{3+}, Fe^{3+}), copper has been used as a dopant in the synthesis of metal-doped TiO_2 expressing reduced band gap and enhanced photocatalytic activity (Yalçın et al. 2010; Kumar and Devi 2011; Yang et al. 2015; Uyguner-Demirel et al. 2018; Turkten et al. 2019; Yu et al. 2019; Moretti et al. 2021; Badawi and Althobaiti 2021). TiO_2 P-25 or sol–gel prepared photocatalyst specimens were frequently used for copper doping via a variety of methods like in situ preparation, wet impregnation, and chemisorption-hydrolysis (Boccuzzi et al. 1997; Bokhimi et al. 1997; Coloma et al. 2000; Colón et al. 2006; Ganesh et al. 2014; Kerrami et al. 2021; Moretti et al. 2021).

TiO_2 photocatalytic degradation of DOM as well as HA was comprehensively studied by Bekbolet and colleagues (Parilti et al. 2011; Uyguner-Demirel and Bekbolet 2011; Uyguner-Demirel et al. 2017). Moreover, molecular size fractions (MSFrs) of HA (100 kDa) and their reactivity towards visible light active TiO_2/ZnO composite photocatalyst specimens were also investigated (Turkten and Bekbolet 2020). Recent interest was diverted to testing Cu-doped TiO_2 prepared by sol–gel method for the photocatalytic removal of HA comprised of MSFrs smaller than 30 kDa (Turkten et al. 2019). The photocatalytic activities of various Cu-doped TiO_2 specimens were evaluated with respect to degradation kinetics of HA in terms of UV–vis and fluorescence spectroscopic parameters and organic contents. Fluorescence properties of HA mapped with excitation emission matrix (EEM) contour plots indicated that the solar photocatalytic degradation pathway was specific for TiO_2-type and Cu-dopant content. A brief literature survey on Cu-doped TiO_2 photocatalysis with respect to preparation methodologies and model compounds was presented emphasizing the importance of humic matter as a substrate (Turkten et al. 2019).

Although UV–vis and fluorescence spectroscopic techniques were widely employed, a few detailed studies have been carried out so far on HA characterization using infrared and Raman spectroscopy as comparative tools along with mineralization extents (Del Vecchio and Blough 2004; Lumsdon and Fraser 2005; Rodríguez et al. 2014a, b; Rodríguez et al. 2016; Wu et al. 2020). Selectivity of different Cu-doped specimens could induce chromophoric changes in humic structure, which could be deduced by specific spectrophotometric parameters. Consequently, assessment of the change in humic MSFrs by multi-method spectroscopic approach such as UV–vis, fluorescence, and ATR-FTIR and SERS spectra would be crucial complementary to previous studies on the photocatalytic degradation of HA.

Use of various TiO_2 specimens such as bare TiO_2 (P-25), sol–gel prepared TiO_2 (synTiO_2), and their respective Cu-doped specimens (i.e., Cu-TiO_2 and Cu-synTiO_2) would possibly lead to the formation of diverse MSFrs upon non-selective/selective degradation mechanism under simulated solar light irradiation. The selectivity of bare and Cu-doped photocatalysts would be comparatively presented focusing on spectroscopic evaluation of humic MSFrs. Considering that humic organic matrix is an integrated pool of dissolved compounds with complex interactions, the main purpose of this study is to understand the photocatalytic behavior of different bare and Cu-doped TiO_2 specimens on MSFr of HA in comparison to initial dark interactions as well as under direct photolytic conditions in the absence of photocatalyst specimens to provide a base-line system description. Therefore, a thorough investigation was performed to elucidate the diversity in molecular size fractionation of HA via application of selected tools as UV–vis (specified ($Color_{436}$, UV_{365}, UV_{280} and UV_{254}), specific (organic carbon based UV–vis parameters) and A_{253}/A_{203} quotient), fluorescence (synchronous scan and excitation-emission matrix contour plots (EEM)), ATR-FTIR, and SERS spectroscopy.

Materials and methods

Materials

HA in the form of Na salt was purchased from Aldrich. Working solution of HA (50 mg/L) was prepared by dilution of the stock solution (1.0 g/L) and used following filtration through a 0.45-μm membrane filter constituting an initial DOC content of 14.50 mg/L. Photocatalyst specimens were TiO_2 P-25, Evonik (TiO_2), sol–gel prepared TiO_2 (synTiO_2), 0.50% Cu doped TiO_2 (Cu-TiO_2), and 0.50% Cu doped synTiO_2 (Cu-synTiO_2). Detailed information on preparation and characterization of the photocatalysts by X-ray diffraction (XRD), Scanning Electron Microscopy in combination with Energy Dispersive X-ray analysis (ESEM-EDAX),

X-ray photoelectron spectroscopy (XPS), Raman spectroscopy, UV–visible diffuse reflectance spectroscopy (UV-DRS), and Brunauer–Emmett–Teller (BET) surface area measurements and Barret–Joyner–Halender (BJH) pore characterization were reported elsewhere (Turkten et al. 2019). Millipore Milli-Q water (with a resistivity of 18.2 MΩ cm at 25 °C) was used as reagent water.

Determination of HA properties

Contents of DOC (mg/L) were quantified as non-purgeable organic carbon via Shimadzu TOC-VWP Total Organic Carbon Analyzer calibrated by using potassium phthalate (range 0–25 mg/L). UV–vis absorption measurements were performed using Perkin Elmer lambda 35 UV–vis Spectrometer using 1-cm quartz cuvettes in wavelength range of 200–600 nm. Fluorescence measurements were carried out by Perkin Elmer LS 55 Luminescence Spectrometer using synchronous and excitation-emission (EEM) mode. Synchronous scan was acquired in the excitation wavelength range of 200–600 nm using the bandwidth of $\Delta\lambda = 18$ nm between the excitation and emission monochromators. EEM fluorescence profiles were obtained by simultaneous incremental changes in both excitation and emission wavelengths. A gradual increase of λ_{exc} from 200 to 500 nm and λ_{emis} from 200 to 600 nm were recorded. Three-dimensional contour plots were derived from data and modelled using MATLAB R2013a program. Attenuated total reflection Fourier transform infrared (ATR-FTIR) measurements were performed using Perkin Elmer Spectrum Two model FTIR equipped with Universal ATR accessory with diamond/ZnSe crystal. All spectra were obtained by 64 scans with a scan resolution of 2 cm^{-1} in the spectral range of 4000–700 cm^{-1}. Prior to each measurement, the crystal was cleaned with ethanol (Sigma-Aldrich) and de-ionized water. Surface-enhanced Raman scattering (SERS) spectra were acquired in the range between 3500 and 100 cm^{-1} by a Thermo Scientific DXR Raman Microscope using Ar^{+} laser excitation at $\lambda = 532$ nm. The laser power and spectral resolution were 10 mW and 2 cm^{-1}, respectively. Silver colloid was prepared according to Lee and Meisel to achieve higher Raman intensity bands (Lee and Meisel 1982).

Characteristic analyses of HA

Prior to and following each treatment, HA was characterized by DOC, specified and specific UV–vis and fluorescence parameters. Specified UV–vis parameters as absorbance values recorded at 436 nm, 365 nm, 280 nm, and 254 nm were designated as $Color_{436}$, UV_{365}, UV_{280}, and UV_{254}, respectively. Specific UV–vis parameters were described as organic carbon based UV–vis (L/mg m) parameters as referred to as $CbColor_{436}$, $CbUV_{365}$, $CbUV_{280}$, and $CbUV_{254}$. Fluorescence intensity recorded at $\lambda_{emis} = 470$ nm was reported as $FI_{sync,470}$ (Bekbolet and Sen Kavurmaci 2015). Fluorescence index (FI) was defined as the ratio of emission intensity at λ_{emis}450 nm to that at λ_{emis}500 nm following excitation at λ_{exc}370 nm. EEM fluorescence features were elucidated by five regions that were ascribed as Region I: Aromatic Proteins I, tyrosine-like (λ_{exc}220-250 and λ_{emis}280-332), Region II: Aromatic Proteins II, tryptophan-like (λ_{exc}220-250 and λ_{emis}332-380), Region III: Fulvic-like (λ_{exc}220-250 and λ_{emis}380-580), Region IV: Microbial byproducts (λ_{exc}250-470 and λ_{emis}280-380), and Region V: Humic-like (λ_{exc}250-470 and λ_{emis}380-580) (Coble 1996; Baker et al. 2008). A pictorial presentation of regional distribution of EEM fluorescence contour plots was illustrated in Supplementary Information (SI) Part 1 Fig. S1. According to above given methodology, FTIR and SERS characterization studies were also performed.

Molecular size fractionation

Following filtration through 0.45-µm and 0.22-µm pore sized membrane filters, HA samples were further fractionated into different MSFrs (Kerc et al. 2004). Sequential stage ultrafiltration through membranes with nominal molecular weight cutoffs as 100 kDa, 30 kDa, 10 kDa, 3 kDa, and 1 kDa, was applied using Amicon model 8010 stirred cell reactor with a total volume of 50 mL. Operating pressures were 1 kg/cm^2 for 100 kDa, 3 kg/cm^2 for 30 kDa, 10 kDa, 3 kDa, and 1 kDa membrane filters. Samples were ascribed as 450 kDa, 220 kDa, 100 kDa, 30 kDa, 10 kDa, 3 kDa, and 1 kDa, respectively.

Treatment schemes

Solar photolytic and photocatalytic experiments were performed using a solar simulator (ATLAS Suntest CPS +) in the wavelength range of 290 nm < λ < 800 nm emitted by an air cooled Xenon lamp. Light intensity (I_o) was measured as 250 W/m^2 with radiometer and $I_o = 1.67$ µE/min in the reaction vessel as determined by ferrioxalate actinometry (Hatchard and Parker 1956). Irradiation period of $t_{irr} = 60$ min was selected to maintain constant exposure conditions to the reaction medium.

Solar photolysis HA solution (50 mg/L) was subjected to irradiation in the Solar Box for a period of 60 min.

Initial adsorption (t = 0 condition) Upon introduction of each of the selected photocatalyst specimen to HA solution under dark conditions, samples were subjected to filtration through 0.45-µm membrane filters. Thus, obtained samples were analyzed for the assessment of the MSFrs as achieved through initial adsorptive interactions.

Solar photocatalysis HA solution (50 mg/L) was subjected to photocatalytic treatment using a constant dose (0.25 mg/mL) of TiO_2, $synTiO_2$, $Cu\text{-}TiO_2$, and $Cu\text{-}synTiO_2$ for a fixed irradiation period of 60 min.

Results and discussion

Humic material is widely known to be composed of both low molecular weight aggregates and high molecular weight fractions expressing a discrete macromolecular behavior in solution. Ultrafiltration technique was employed to explore molecular heterogeneity thus polydispersity of HA under various conditions within bulk humic matter. Owing to complexity of initial HA, offline characterization of fractionated material was also presented.

Characteristic analyses of HA molecular size fractions

Due to the presence of a large quantity of aromatic condensation and related conjugated π systems in HA structure, UV–vis spectra would be devoid of any particular absorption band. Therefore, direct quantification would not be possible although spectral characterization of a particular chromophore region would bring significant structural information. UV–vis spectroscopic analysis of HA was performed subsequent to fractionation and displayed the following specified parameters and DOC (Fig. 1a) as well as specific parameters and A_{253}/A_{203} quotient (Fig. 1b). It should be clearly indicated that each fraction was composed of all lower MSFrs.

Specified UV–vis parameters revealed the following information with respect to decreasing molecular size:

450 kDa and 220 kDa fractions were not significantly different from each other.
100 kDa fraction expressed almost 50% reduction in all UV–vis parameters.
30 kDa and 10 kDa fractions were not significantly different from each other expressing 25% reduction from 100 kDa in all UV–vis parameters.
3 kDa and 1 kDa fractions expressed almost 50% difference in between color forming moieties and UV absorbing centers. All specified parameters were quite low in comparison to 10 kDa fraction.

DOC contents displayed an almost logarithmic decreasing profile with respect to decreasing molecular size. Accordingly, specific UV–vis parameters displayed MSFr specific variations. $CbUV_{254}$ (L/mg m) was generally accepted as an indicator of hydrophobicity/hydrophilicity and aromaticity of organic matter in water (Langhals et al. 2000; Johnson et al. 2002; Hua et al. 2020). The relationship between MSFrs of HA and aromatic carbon contents showed that $CbUV_{254}$ gradually decreased with MSFr with the exceptions of 220 kDa and 10 kDa. However, $CbColor_{436}$ (L/mg m) parameter displayed minor variations with respect to decreasing order of molecular size signifying that color forming moieties were evenly distributed within the DOC pool of each MSFr. The inconsistency in between these two specific parameters, i.e., $CbUV_{254}$ and $CbColor_{436}$ could be attributed to the variations in content of color forming moieties composed of conjugated π-π systems and hetero atoms with lone pair of electrons and dense aromatic skeleton. $CbUV_{365}$ as related to molecular size heterogeneity and $CbUV_{280}$ as related to double bond system were expected to follow a similar trend with regard to $CbColor_{436}$ and $CbUV_{254}$.

Although absorbance value at $\lambda = 254$ nm has been widely employed as a surrogate parameter of DOC contents of DOM, absorbance at $\lambda = 203$ nm has not been considered so far. More specifically, UV absorption spectra of HA exhibited an absorption band at 253 nm related to the electron-transfer band, whereas 203 nm absorption band was related to benzenoid band due to vibrational perturbations in the π- electron system of humic. As an indicator of unsaturated /saturated fraction proportions in organic matrix, A_{253}/A_{203} quotient could also express the abundance of substituted functional groups linked to aromatic structures where higher ratios corresponded to aromatic rings that contain carbonyl, carboxyl, hydroxyl, and ester groups, and lower ratios corresponded to aliphatic chains (Korshin et al. 1997; Zhang et al. 2016). As representative sub-units of humics, catechols, and related phenolic pure compounds, the quotient of A_{253}/A_{203} is typically between 0.25 and 0.35, whereas for aromatic rings substituted with carbonyl, carboxyl and (especially) ester carboxylic groups, the A_{253}/A_{203}, quotient may be significantly above 0.40 (Scott 1964). Nevertheless, A_{253}/A_{203} quotient would be low for DOM in which the aromatic rings were substituted predominantly with aliphatic functional groups and would increase for DOM in which the aromatic rings were highly substituted with hydroxyl, carbonyl, ester, and carboxyl groups. Thus, A_{253}/A_{203} quotient might be a good indicator of the tendency for humic molecules to participate in adsorption or complexation reactions although a possible error due to absorption of inorganic ions such as nitrates or sulfates around 200 nm should also be encountered (Kim and Yu 2005; Her et al. 2008). The A_{253}/A_{203} quotient could also be correlated with the reactivity of humics towards oxidizing agents. Humic acid (Aldrich) presented a high A_{253}/A_{203} quotient ($1.5 < x < 4.5$) for the low molecular weights (< ~1500 Da), $0.7 < x < 1.5$ for the intermediate molecular weights (~1500 Da < x < ~13,000 Da), and a low quotient (< 0.7) for the high molecular weights (> ~13,000 Da)

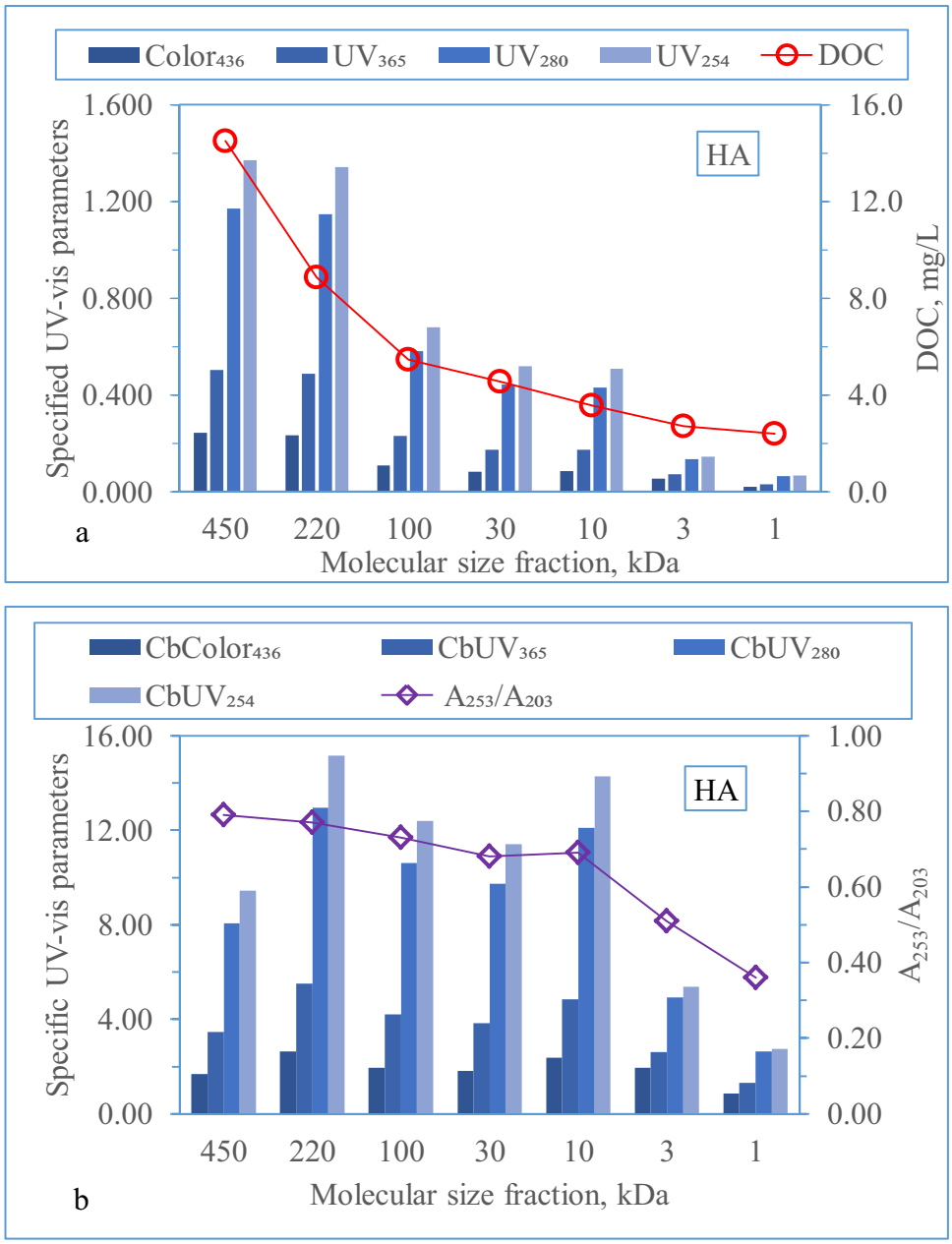

Fig. 1 (**a**) Specified UV–vis parameters and DOC (mg/L), (**b**) and specific UV–vis parameters (L/mg m) and A_{253}/A_{203} quotient of HA

(Pitois et al. 2008). A_{253}/A_{203} quotient displayed a steady decrease with minor variations (0.79–0.68) for all MSFrs greater than 10 kDa fraction followed by a steep decrease for 3 kDa (0.51) and 1 kDa (0.36) fractions that were composed of considerably lower DOC (< 3 mg/L) contents. The changes in the A_{253}/A_{203} quotient suggested that aromatic rings substituted with various functional groups were structurally altered within each MSFr. The quotient decreased with decreasing MSFr and depended more on the phenolic group content rather than the carboxylic group content in the humic structure.

Treatment of HA

Prior to application of photocatalysis, preliminary experiments were implemented: (i) photolytic conditions that were carried out in the absence of photocatalyst specimens for a period of 60 min, and (ii) t = 0 condition representing initial adsorptive interactions of photocatalysts in the absence of light. Photocatalysis was carried out using one of the following; TiO_2, synTiO_2, Cu-TiO_2 and Cu-synTiO_2 specimens for an irradiation period of 60 min. Since UV–vis absorption profiles of HA were highly dependent on molecular weight/

size, aromatic/aliphatic quotient as well as DOC content, molecular size distribution profile could be compared under specified experimental conditions.

Solar photolysis

In the aquatic environment, DOM is ubiquitous and acts both as a photosensitizer and a quencher. The photosensitizing properties are due to production of triplet DOM (^{3}DOM) and reactive oxygen species (ROS (i.e., $O_2^{\bullet-}$, $^\bullet$OH, and H_2O_2) along with excited states of DOM* have been explained in detail elsewhere (Dalrymple et al. 2010; Loiselle et al. 2012).

Triplet DOM reactivity is mainly attributed to excitation of aromatic ketones, aldehydes, and quinone moieties. In aqueous reaction medium and under solar irradiation, HA could also operate similarly. Although very slight degradation thereby loss of organic carbon was envisaged, variations in spectroscopic properties were expected due to intra- and inter- molecular rearrangements. Upon solar photolysis of HA and following molecular size fractionation, UV–vis absorbance analysis was performed and displayed as specified parameters and DOC (Fig. 2a) and specific parameters and A_{253}/A_{203} quotient (Fig. 2b).

Upon solar photolysis, specified UV–vis parameters revealed the following information with respect to decreasing molecular size:

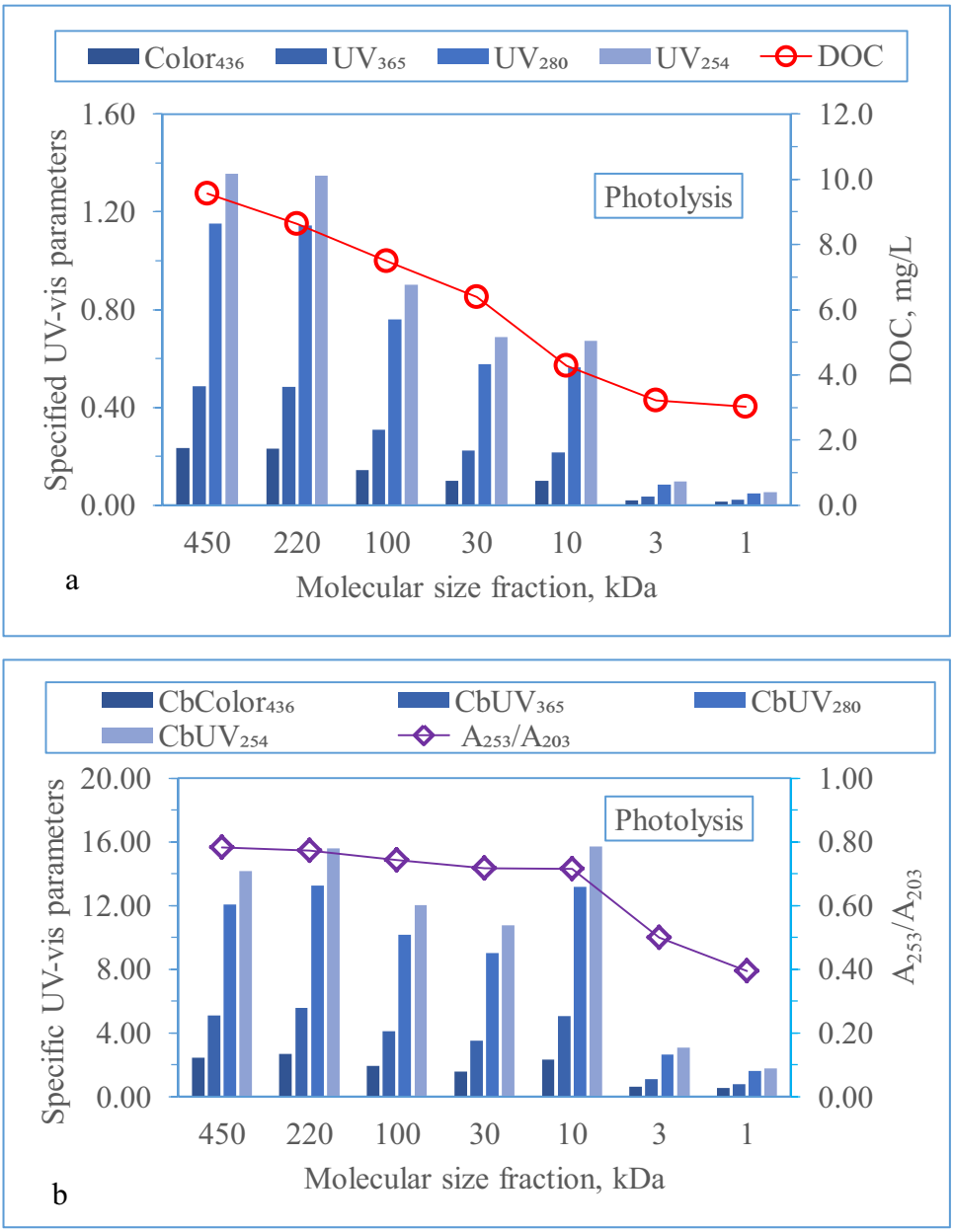

Fig. 2 (**a**) Specified UV–vis parameters and DOC (mg/L), (**b**) and specific UV–vis parameters (L/mg m) and A_{253}/A_{203} quotient of HA upon solar photolysis

450 kDa and 220 kDa MSFrs were not significantly different from each other.
100 kDa fraction expressed almost 40% reduction in all UV–vis parameters.
30 kDa and 10 kDa MSFrs were not significantly different from each other expressing almost 25% reduction from 100 kDa in all UV–vis parameters.
3 kDa and 1 kDa MSFrs expressed significant reductions in all UV–vis parameters in comparison to 10 kDa fraction.

From a general perspective, a comparison to initial conditions (450 kDa MSFr) revealed insignificantly different trend that could be mentioned although slight variations in all specified UV–vis parameters were recorded (Fig. 2a). However, molecular size dependent DOC profile indicated variations in comparison to UV_{254} that was regarded as a surrogate parameter of DOC (Edzwald et al. 1985). Accordingly, specific prameters expressed slight variatons followed by a decrease in lower MSFrs < 10 kDa (Fig. 2b). The A_{253}/A_{203} quotient displayed a steady decrease with insignificant variations for all MSFrs greater than 10 kDa fraction followed by a steep decrease for 3 kDa (0.5) and 1 kDa (0.4) fractions that were composed of considerably lower DOC (< 3 mg/L) contents.

Initial adsorption, t = 0 condition

Adsorption of the substrate at the surface of the photocatalyst is considered as an essential step that determines the interaction of photon generated ROS with the substrate molecules. Initial adsorption, i.e., t = 0 min condition represented the instantaneous introduction of the photocatalyst particle to HA solution and its subsequent removal by filtration through a 0.45-μm membrane filter. Surface interactions could be visualized as governed by simultaneously operating attractive and repulsive forces between deprotonated functional groups of the adsorbate (HA macromolecular oxyanion size fractions) and photocatalyst surface acquiring both charges (Turkten et al. 2019). Tanaka 2012 reported that HA MSFr greater than 100 kDa would acquire more aliphatic COOH (and OH), while those in the range of 100–30 kDa MSFr comprised more aromatic COOH. Although no information on MSFrs smaller than 30 kDa was reported, in either case under the working pH conditions, all carboxylic groups would be expected to be deprotonated excluding OH functional groups (Tanaka 2012). However, possibility of lateral electrostatic repulsions between adsorbed HA fractions and HA MSFrs present in the bulk and exclusion of all conformational variations in macromolecular sub-fractions even sections protruding to the solution should also be encountered. Under these conditions, HA should not be recognized as truly polymeric expressing regular repetition of simple units, since discrete variations in MSFr would certainly affect the extent of surface coverage. Based on these conditions, the extent of adsorption was accepted as an indicator of the surface coverage prior to photocatalysis upon initiation of irradiation.

Considering the structural diversity of the different MSFrs of HA and their interactions with various photocatalyst specimens, UV–vis spectroscopic properties of HA MSFrs as normalized to the data of 450 kDa fraction could be developed for understanding of the interactions prevailing under dark conditions. As presented by Turkten and colleagues, the exposed surface was dependent on surface area of each photocatalyst specimen (constant dose 0.25 mg/mL). BET surface area (m^2/g) variations of the photocatalyst specimens were arranged in a descending order as follows: TiO_2 (57.56) > $synTiO_2$ (50.25) > Cu-TiO_2 (46.50) > Cu-$synTiO_2$ (44.22). On the other hand, surface charge development was also pH_{zpc} dependent expressing a decreasing order as follows: Cu-TiO_2 (6.47) > TiO_2 (5.67) > $synTiO_2$ (4.91) > Cu-$synTiO_2$ (4.22) Since the pH of reaction medium was almost neutral (pH = 6–7), TiO_2 and Cu-TiO_2 of the photocatalyst specimens could acquire comparatively more positively charged sites in comparison to $synTiO_2$ and Cu-$synTiO_2$ (Turkten et al. 2019). Moreover, pore volume (cm^3/g) characteristics could also be listed as follows: $synTiO_2$ (0.169) > TiO_2 (0.150) > Cu-$synTiO_2$ (0.0938) > Cu-TiO_2 (0.0512) expressing insignificant effect on dark surface interactions. From a general perspective based on this system description, the following initial adsorption trends were attained.

Upon introduction of TiO_2, the specified UV–vis parameters followed the sequence as follows:

450 and 220 kDa MSFrs were quite similar as 14–15% removal in all UV–vis parameters,
100 kDa fraction was significantly removed almost 40–45% as expressed by all UV–vis parameters,
30 kDa and 10 kDa MSFrs displayed 60–68% adsorption efficiency for all UV–vis parameters,
3 kDa and 1 kDa fractions expressed variations as $UV_{254} > UV_{280} > UV_{365} > Color_{436}$ being 1 kDa MSFr significantly higher in comparison to 3 kDa fraction.

Upon introduction of $synTiO_2$, the specified UV–vis parameters followed the trend as follows:

450 and 220 kDa MSFrs displayed slightly different (< 5%) removals in all UV–vis parameters,
100 kDa fraction displayed significant removal as 35–40% of all UV–vis parameters,
30 kDa and 10 kDa MSFrs were quite similar 65–72% removals in all UV–vis parameters,

3 kDa and 1 kDa MSFrs expressed variations as $UV_{254} > UV_{280} > UV_{365} > Color_{436}$ as 79–95% being 1 kDa fraction more significant in comparison to 3 kDa fraction.

Upon introduction of Cu-TiO_2, the specified UV–vis parameters followed the trend as follows:

450 and 220 kDa MSFrs were slightly different (1–7%) in all UV–vis parameters,
100 kDa fraction displayed almost 48–56% of all UV–vis parameters,
30 kDa fraction displayed 50% removal of all UV–vis parameters,
10 kDa fractions were quite similar as almost 75% in all UV–vis parameters,
3 kDa fraction was removed as expressed in a decreasing order of $UV_{254} > UV_{280} > UV_{365} > Color_{436}$,
1 kDa fraction expressed very slight variation as almost equal to 5%.

Upon introduction of Cu-synTiO_2, the specified UV–vis parameters followed a similar trend in all UV–vis parameters:

450 and 220 kDa MSFrs were slightly different (1–3%) in all UV–vis parameters.
100 kDa fraction displayed almost 36–40% of all UV–vis parameters,
30 kDa fraction displayed 46–50% removal of all UV–vis parameters,
10 kDa fractions were quite similar as almost 53–57% in all UV–vis parameters,
3 kDa fraction was removed as expressed by quite similar in all UV–vis parameters,
1 kDa fractions expressed very slight variations as almost equal to 5–8%.

All of the specific UV–vis parameters displayed molecular size dependent variations through surface interactions with different photocatalyst specimens. Upon use of TiO_2, all parameters expressed almost similar tendencies excluding the smaller size fractions as 3 kDa and 1 kDa fractions. These fractions expressed similarities in UV absorbing centers in comparison to color forming moieties within the respective DOC pool. For simplicity purposes, $CbColor_{436}$ and $CbUV_{254}$ were also comparatively discussed. $CbColor_{436}$ expressed the following decreasing trend with respect to photocatalyst specimen and HA MSFr: Cu-TiO_2: 3 kDa (5.36) > TiO_2: 3 kDa (4.23) > Cu-synTiO_2: 220 kDa (3.00) > HA: 220 kDa (2.63) > synTiO_2: 100 kDa (2.54). On the other hand, $CbUV_{254}$ displayed the following descending trend with respect to photocatalyst specimen and HA MSFrs although variations in between them could be considered as insignificant: Cu-TiO_2: 220 kDa (19.6) > Cu-synTiO_2: 220 kDa (16.9) > TiO_2: 10 kDa (15.6) > synTiO_2: 100 kDa (15.3) > HA: 220 kDa (15.1). Upon use of TiO_2, 10 kDa size fraction expressed the highest values for $CbUV_{254}$ and $CbUV_{280}$. In the presence of synTiO_2, 100 kDa size fraction was the most prominent for all specific UV–vis parameters. However, for Cu doped photocatalysts, 220 kDa molecular size fractions dominated over the other fractions for all specific UV–vis parameters.

In general, a steady decrease of A_{253}/A_{203} quotient with decreasing MSFr irrespective of the photocatalyst specimen type was recorded (Fig. 2b) Upon introduction of TiO_2, a slightly decreasing trend followed by a sharp decrease for 3 kDa and 1 kDa fractions was obtained. Although a similar trend was attained for synTiO_2, 3 kDa fraction expressed comparatively lower A_{253}/A_{203} indicating the role of aromatic moieties. The role of Cu-doping could be deduced as similar to respective trend of undoped TiO_2 specimen with a distinction of 100 kDa fraction being lower than 220 kDa and 30 kDa fractions followed by a drastic decrease from 0.60 to 0.35 for 3 kDa and 1 kDa MSFrs, respectively. Upon use of Cu-synTiO_2, a minor decrease (0.79 to 0.69) was recorded for 450 to 10 kDa MSFrs followed by a sharp decline to 0.30 for 1 kDa MSFr. It should also be mentioned that almost all of the A_{253}/A_{203} quotients were lower than those presented by Pitois and colleagues (Pitois et al. 2008).

Photocatalysis

Upon solar irradiation, the following reactions (1–3) would take place in the presence of semiconductor species (SC) (Uyguner and Bekbolet 2007; Li et al. 2016; Turkten et al. 2019).

$$^3DOM^* + H_2O \rightarrow DOM - H^* + HO^\bullet \quad (1)$$

$$^3DOM^* \rightarrow {}^3DOM^{\bullet+}e^- \quad (2)$$

$$DOM^* + SC + h\nu \rightarrow DOM^{\bullet+} + SC(e^-) \quad (3)$$

Under these oxidative conditions, DOM MSFrs would certainly express diverse affinities either by self-inter/intra transformation, or by degradation via loss of DOC.

UV–vis spectroscopic evaluation

Photocatalytic degradation of HA was performed using selected photocatalysts and humic structural changes were evaluated in a similar trend (Fig. 3). Specified and specific UV–vis spectroscopic properties of HA MSFrs upon photocatalytic treatment using TiO_2 based specimens were

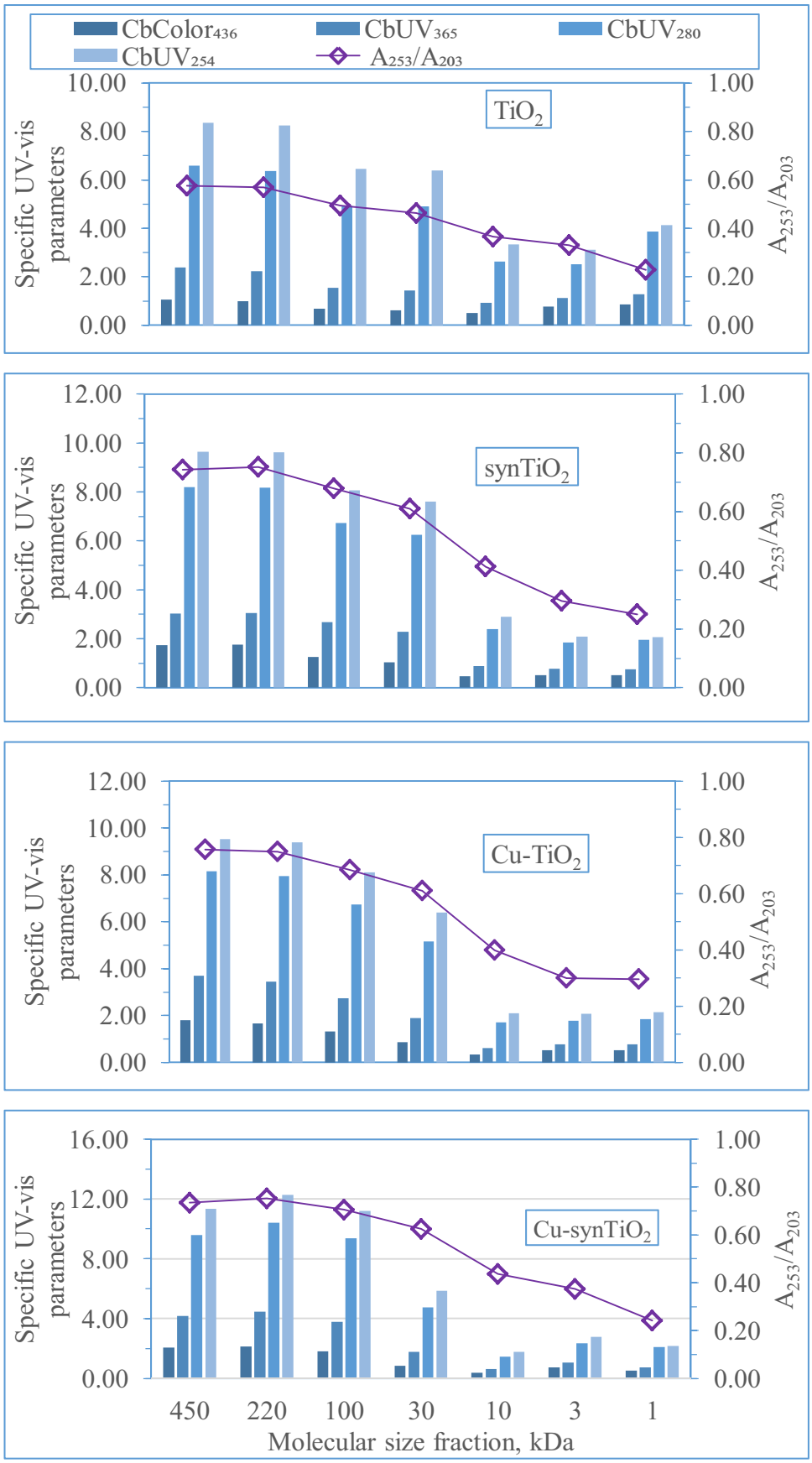

Fig. 3 Specific UV–vis parameters (L/mg m) and A_{253}/A_{203} quotient of HA upon photocatalysis using TiO_2, $synTiO_2$, Cu-TiO_2, and Cu-$synTiO_2$

evaluated and specified UV–vis parameters were illustrated in Table S1 (SI Part 1).

Photocatalytic performance of TiO_2 was significantly evident in comparison to all other specimens in MSFrs < 10 kDa. Affinities of $synTiO_2$ as well as Cu-doped specimens could be recognized as non-specific with respect to each MSFr and specified UV–vis parameter.

Specified UV–vis parameters could better be envisioned by normalization to respective DOC contents as expressed by specific UV–vis parameters (Fig. 3). Comparative evaluation of $CbUV_{254}$ illustrated that $synTiO_2$ and $Cu\text{-}TiO_2$ behaved similarly. Irrespective of the photocatalyst used, significant decrease of $CbUV_{254}$ was evident for size fractions < 10 kDa. Upon use of TiO_2, $CbColor_{436}$ decreased gradually down to 10 kDa, for lower MSFrs an increasing trend was attained. From photocatalyst specimen point of view, differences were notable for 450–10 kDa size fraction; however, for lower MSFrs (3 kDa-1 kDa), insignificant variations could be indicated.

Following initial adsorption and light exposure, during photocatalysis substantial change of A_{253}/A_{203} quotient would be expected. A continuous almost linear decrease of A_{253}/A_{203} (0.58–0.23) for all MSFrs was attained by TiO_2 photocatalysis. Upon $synTiO_2$ photocatalysis, a rather smooth declining feature was attained for higher MSFrs, exhibiting a sharp decrease for 100–30 kDa fractions followed by a decreasing profile for lower MSFrs. Cu doping of TiO_2 and $synTiO_2$ affected the descending profile of A_{253}/A_{203} almost similarly for lower MSFrs being more pronounced for $Cu\text{-}synTiO_2$. As expressed for t = 0 condition, almost all A_{253}/A_{203} values displayed the predominant role of aromatic moieties with respect to aliphatic groups. The changes in A_{253}/A_{203} quotients were mainly attributed to the presence of the aromatic skeleton dominated by functional groups in response to removal and generation during oxidative degradation simultaneously resulting in a substantial loss of DOC. Formation of lower MSFrs via degradation and/or depolymerization of organic matrix could be related to non-selective action of ROS with humic MSFrs even leading to the formation and accumulation of smaller molecules that were nonchromatic (Thomson et al. 2004; Turkten et al. 2019). However, gross parameters could not directly indicate any apparent increase in any particle size fraction due to continuously operating non-selective oxidation mechanism of •OH as well as reactions of other ROS species.

A continuous declining feature of A_{253}/A_{203} was attained for all humic MSFrs expressing molecular sizes greater than 10 kDa. Within this framework, surface of $Cu\text{-}TiO_2$ was more prone to preferential adsorption of UV absorbing centers. Lower MSFrs (3 kDa and 1 kDa) of HA expressed distinctly different tendencies towards surface active sites of the photocatalyst specimens. The most remarkable variation was attained for 3 kDa fraction the outcome of which could be expressed as a decreasing trend: $Cu\text{-}TiO_2 > TiO_2 > synTiO_2 > Cu\text{-}synTiO_2$. Furthermore, 1 kDa fraction expressed almost similar A_{253}/A_{203} quotient (≈ 0.36) with an exception of 0.30 upon introduction of $Cu\text{-}synTiO_2$.

A slightly decreasing trend of A_{253}/A_{203} quotient was attained for all humic MSFrs upon photolysis expressing molecular sizes greater than 10 kDa that could be regarded as similar to HA. Upon photocatalysis, TiO_2 displayed a rather consistent trend (0.58 to 0.30) whereas $synTiO_2$, $Cu\text{-}TiO_2$ and $Cu\text{-}synTiO_2$ followed a similar behavior with respect to decreasing molecular size. As previously reported, size of MSFRs could well correlate with the respective pore size of the photocatalyst specimens. With respect to BJH pore diameters, diverse MSFrs could be located within mesoporous pore structures, i.e., TiO_2 less than 100 kDa, $synTiO_2$ less than 10 kDa, $Cu\text{-}synTiO_2$ less than 3 kDa. Owing to lower pore diameter of $Cu\text{-}TiO_2$, insignificant interaction through pores could be expected (Turkten et al. 2019).

As presented previously, the selected photocatalyst specimens exerted different affinities towards HA in terms of specified UV–vis parameters excluding almost similar mineralization rates (Turkten et al. 2019). From fundamental point of view, absorbed light intensity is directly related to the mechanism and kinetics of photocatalysis (Emeline et al. 2000). The resulting effect could be envisaged in diversity of HA MSFrs and respective descriptive parameters.

Aromaticity and functionality of humic acid could well be represented by A_{253}/A_{203} quotient. Additionally, $CbUV_{254}$ indicated hydrophobicity/hydrophilicity and aromaticity. Accordingly, HA MSFrs expressed a positive correlation between A_{253}/A_{203} quotient and $CbUV_{254}$ ($R^2 = 0.719$) under all conditions covering initial, photolytic, initial adsorption, and photocatalysis. Photocatalyst type revealed insignificant effect on correlation for all HA MSFrs (Fig. 4).

Synchronous scan fluorescence features and EEM fluorescence contour plots

System-based comparisons of the synchronous scan fluorescence features and EEM fluorescence contour plots were presented in respective figures (SI Part 2 Fig. S3 and SI Part 1 Fig. S2). HA displayed a major peak at λ_{emis}470 nm (± 10 nm) that could be considered as expressing almost similar fluorescence intensities ($FI_{sync,470}$) for MSFrs 450–100 kDa followed by a decreasing profile for 100 kDa MSFr. For smaller MSFrs (< 30 kDa), a non-consistent trend was attained in $FI_{sync,470}$. A shoulder–like peak was also observed at around λ_{emis}400 nm following a decreasing trend in accordance with decreasing molecular size. On the other hand, variable distribution of fluorescence intensities was evidently recorded in λ_{emis} range of 200–600 nm. Moreover, little is known at the molecular level about the

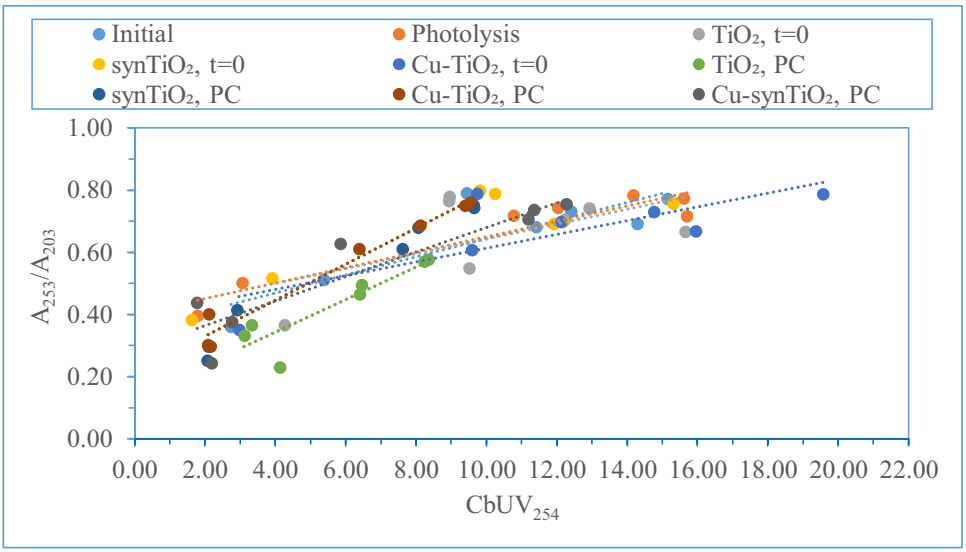

Fig. 4 Correlation between A_{253}/A_{203} quotient and $CbUV_{254}$ of HA MSFrs under all conditions

nature of the constituents or interactions that produce these rather unique spectral features. Upon exposure to irradiation, HA displayed a major peak at λ_{emis}470 nm that could be considered as following an inconsistent trend with respect to decreasing molecular size. Both the shoulder–like peak at around λ_{emis}400 nm and variable distribution of fluorescence intensities in λ_{emis} range of 200–600 nm were also evident. The most noteworthy difference was attained in both 100 kDa and 30 kDa MSFrs expressing considerably higher fluorescence intensities in the emission range of 200–600 nm (SI Part 2 Fig. S3).

Upon instantaneous introduction of TiO_2 to HA solution, each MSFr expressed almost similar tendencies towards surface active sites for electrostatic attractions excluding 10 kDa fraction (SI Part 2 Fig. S3). In the presence of $synTiO_2$, each MSFr was attracted to the surface in a decreasing order of λ_{emis}470 nm excluding 100 kDa and 30 kDa fractions of which fluorescence profiles reflected an almost coinciding behavior. Fluorescence intensities recorded at $\lambda_{emis} < 400$ nm displayed practically similar tendencies. Cu doping of both TiO_2 and $synTiO_2$ could disturb fluorescence patterns due to possibility of complexing tendency of substitutional lattice of Cu^{II} and/or Ti^{IV} atoms under dark conditions. The role of preparation methodology of TiO_2 and $synTiO_2$ could also be encountered with respect to physicochemical properties (Turkten et al. 2019). The peak maxima at 385 nm is evident both in the presence of Cu-TiO_2 and Cu-$synTiO_2$ for high MSFrs (450 kDa and 220 kDa). However, there was a shift of maxima to 400 nm for 100 kDa fraction that gradually decreased with decreasing molecular size. More significantly, the fluorophores recorded in λ_{emis}200–300 nm region were completely removed as a result of surface adsorption.

As previously presented, upon TiO_2 photocatalysis, a remarkable shift to lower emission wavelengths was attained for all MSFrs in accordance with DOC removal (SI Part 2 Fig. S3). More significantly, due to the formation of lower MSFrs, considerably higher fluorescence intensities were recorded for 3 kDa and 1 kDa MSFrs. In comparison to TiO_2, $synTiO_2$ displayed a noteworthy difference that could be visualized by the emergence of fluorophores at λ_{emis}300 nm for MSFrs < 30 kDa (following an intensity order as 1 kDa > 3 kDa > 10 kDa) although no significant fluorophores were detected for either initial HA or HA upon introduction of $synTiO_2$. Since DOC removal was considerably lower in comparison to TiO_2 photocatalysis under the specified experimental conditions, it could be deduced that intramolecular rearrangements and conformational changes could possibly lead to dissimilar performance. Cu-TiO_2 photocatalysis displayed the removal of all fluorophores in almost a consistent trend along with the emergence of new fluorophores at λ_{emis} 300 nm more specifically for 3 kDa and 1 kDa fractions with considerably higher fluorescence intensities. The reason could be attributed to the formation of lower MSFrs through non-selective oxidation mechanism. Moreover, an accumulation around λ_{emis} = 350–400 nm region with a peak around λ_{emis}375 nm should also be encountered.

A comparative evaluation of the synchronous scan fluorescence spectral features of Cu doped specimens could be assessed by disassembling of the accumulation around λ_{emis} = 350–400 nm region. In a similar manner, fluorescence intensities at λ_{emis}300 nm ($FI_{sync} > 30$) followed an order as 1 kDa > 3 kDa > 10 kDa in MSFrs in comparison to fluorescence intensities ($FI_{sync} > 10$) recorded for higher MSFrs. Besides general evaluation of the synchronous scan fluorescence spectral patterns recorded for all HA MSFrs under all specified experimental conditions, as the indicative major $FI_{sync,470}$ values were also presented in a comparative manner (Fig. 5). Exposure to irradiation did not affect $FI_{sync,470}$ of 100 kDa fraction contrary to the consistent trend attained for other MSFrs.

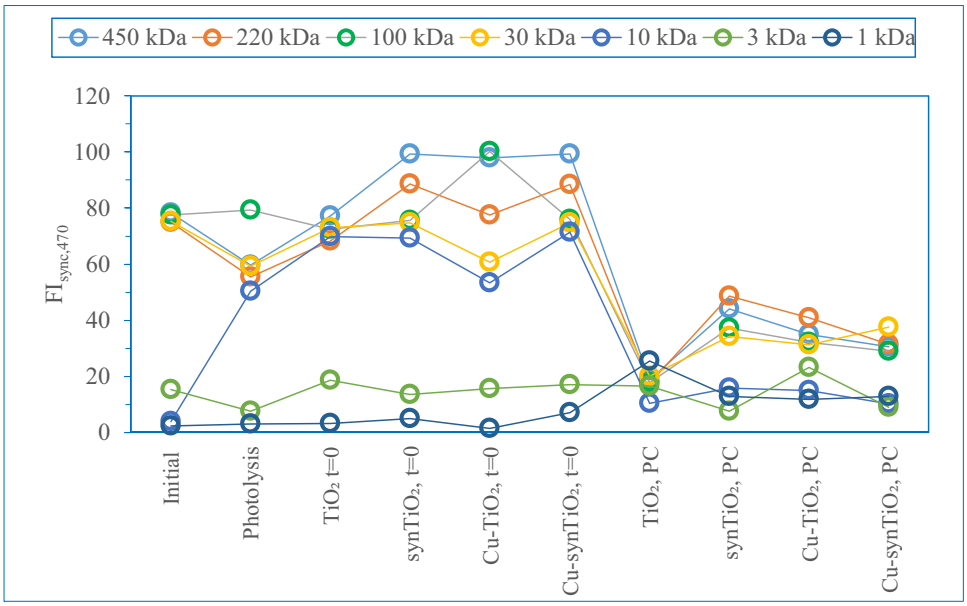

Fig. 5 $FI_{sync,470}$ variations of HA MSFrs under the specified conditions (PC signifies photocatalysis)

Initial surface attractions resulted in a division in MSFrs as group 1 as 10–450 kDa and group 2 as 3 kDa and 1 kDa fractions. Since group 2 fractions displayed almost similar $FI_{sync,470}$ values, the main fluorophore groups affecting the initial adsorptive interactions should be related to group 1 as comprised of higher MSFrs. It should also be indicated that the whole fluorescence spectral features should also be considered along with the remaining UV absorbance and DOC contents (Korak et al. 2014). The most striking point was attained upon TiO_2 photocatalysis, at which all MSFrs expressed almost similar fluorescence intensities in the range of 25.5–16.6. It should be noted that higher MSFrs were mineralized or transformed to lower MSFrs along with DOC removals. Following photocatalysis, subsequent formation of higher 450 kDa, and 220 kDa MSFrs through recombination and/or polymerization via radical mechanism should not be considered.

Almost under all conditions, lower MSFrs ($\leq$ 10 kDa) exhibited considerably lower $FI_{sync,470}$ ($<$ 25) during photocatalysis. Non-selective oxidation mechanism distinctly affected MSFrs in terms of $FI_{sync,470}$ parameter emphasizing the discrimination of degradation pathways proceeding either on direct surface of the photocatalyst or in close vicinity of the surface depending on the type of ROS species. Cu doping of either TiO_2 or $synTiO_2$ did not represent any significant effect in comparison to initial $synTiO_2$ indicating the selective effectiveness of higher MSFrs.

Moreover, FI values of all HA MSFrs (0.96–1.5) were compared to respective humic FI values under all conditions (Fig. 6). Upon photolysis, no significant variation was observed for all MSFrs (Hansen et al. 2016). Upon initial adsorption, all MSFrs excluding 1 kDa fraction displayed almost similar FI values through a stepwise increase as "450 kDa-220 kDa," "100 kDa-10 kDa," and a steep increase. On the other hand, all photocatalyst specimens expressed almost similar tendencies with minor changes for Cu-TiO_2 most probably due to presence of substitutional Cu on the TiO_2 surface.

Upon photocatalysis, extensive variations were observed for all MSFrs and photocatalyst specimens. TiO_2 photocatalysis resulted in substantial increase of FI for MSFrs greater than 10 kDa fraction in comparison to initial HA. On the other hand, Cu doping of $synTiO_2$ displayed comparatively higher FI values for MSFrs smaller than 10 kDa. Furthermore, the effect of $synTiO_2$ photocatalysis was more pronounced in comparison to TiO_2 and Cu-doped respective counterparts.

Three-dimensional images have revealed the entire domain of excitation/emission spectra for humic fractions (SI Part 1 Fig. S2). It should also be noted that fluorescence spectral overlaps in 3D-EEM might hinder an accurate evaluation of the changes in different fluorophores. Compared to Fig. 5, a non-specific correlation with synchronous scan fluorescence spectral features could be expressed due to concurring behavior of fluorophores.

EEM fluorescence contour plots of HA displayed humic-like (Region V) and fulvic-like (Region III) fluorophoric regions and were devoid of Regions I, II, and IV that were related to aromatic proteins and microbial by-products for MSFrs of 450 kDa to 10 kDa. Lower MSFr as 3 kDa expressed a decreasing profile of Region III and almost complete removal of Region V. Moreover, 1 kDa fraction expressed a shift to regions I and II and no indication of other regions were detected. Upon solar irradiation of HA, EEM fluorescence contour plots significantly displayed the presence of Region III and V and were lacking

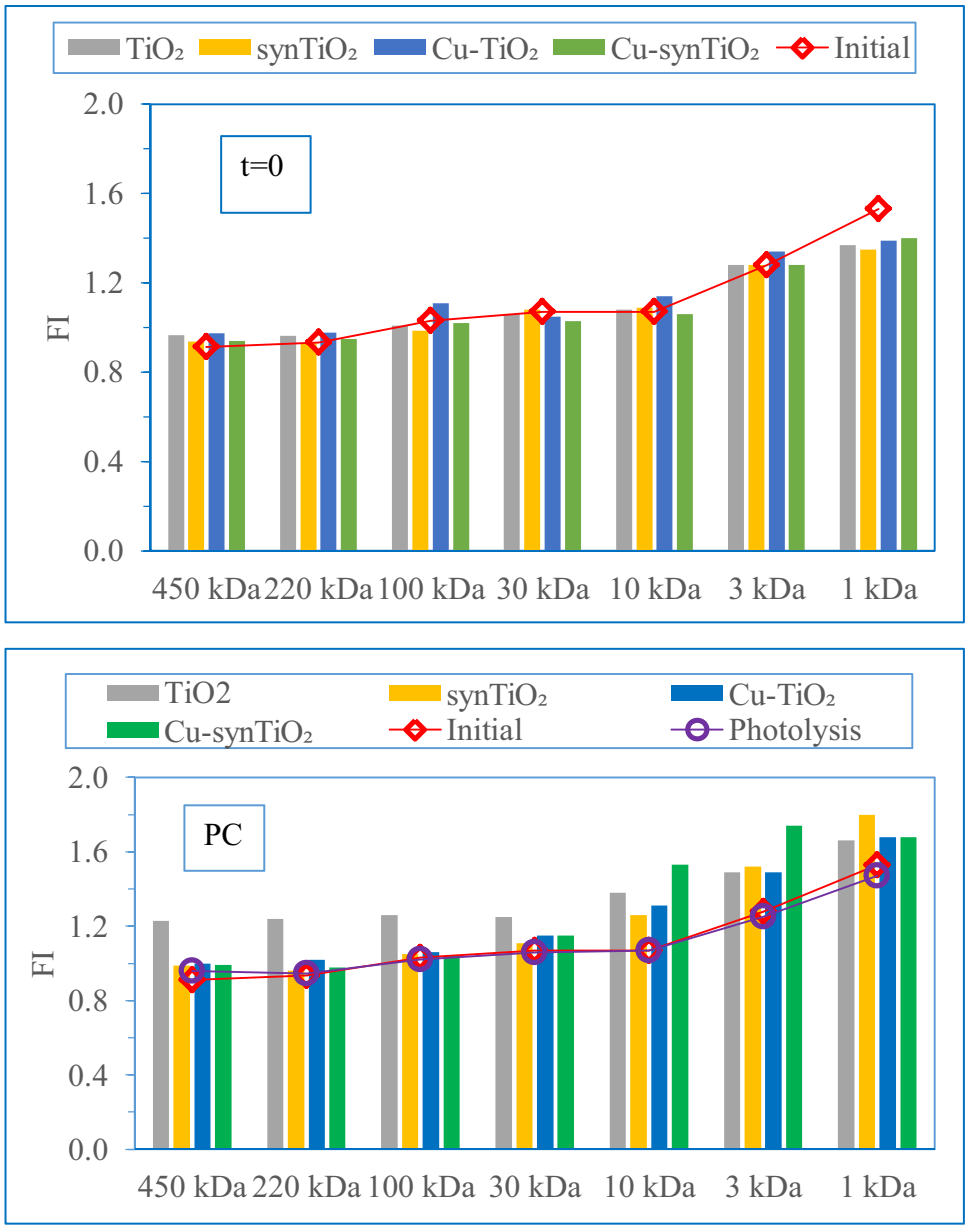

Fig. 6 FI variations of HA MSFrs under photolysis and photocatalytic oxidation conditions with respect to initial HA (PC signifies photocatalysis)

of Regions I, II, and IV as were detected for initial HA. MSFr of 3 kDa expressed a decreasing profile of Region III and partial removal of Region V. A slight shift to Regions I and II and absence of other regions were visualized for 1 kDa fraction. From a general perspective, EEM fluorescence contour plots of initial HA and HA upon photolysis displayed considerably similar trends. In both of the profiles, Region III and IV were evident and Regions I, II, and IV were absent for MSFrs > 10 kDa. 3 kDa MSFr expressed a fading profile of Region III and Region V. Red coloration of 100 kDa, 30 kDa, and 10 kDa was significant for HA, while 30 kDa and 10 kDa MSFrs were more intense in fluorescence intensity upon photolysis.

Upon introduction of TiO_2 to HA, EEM fluorescence contour plots of all MSFrs were similar to both initial and photolytic conditions in terms of regional distribution excluding intensity factor. More significantly, 3 kDa fraction displayed the presence of Regions I-III whereas 1 kDa fraction displayed the presence of Regions I and II. Intense red coloration indicating higher fluorescence intensity was more dominant for 30 kDa MSFr. Likewise, upon introduction of $synTiO_2$ to HA EEM fluorescence contour plots of all MSFrs were similar to both initial and photolytic conditions. The presence of Region III was still evident for 3 kDa MSFr and more significantly, 1 kDa fraction displayed the presence of Regions I and II. The presence of Cu in TiO_2

matrix was more effective for 100 kDa MSFr under t = 0 condition in intensity of both Regions III and V. However, lower MSFrs displayed almost similar EEM fluorescence contour plots. Effect of Cu-doping of synTiO_2 was similar to undoped synTiO_2 MSFr in intensity of both Regions III and V. Lower MSFrs displayed almost similar EEM fluorescence contour plots.

Upon TiO_2 photocatalysis, mainly Regions III and V were evident for 450–10 kDa fractions. Lower MSFrs displayed complete absence of humic-like and fulvic-like regions expressing initially the fluorophoric regions of I and II. Upon synTiO_2 photocatalysis, mainly Regions III and V were evident for 450–10 kDa fractions. Lower MSFrs displayed complete absence of humic-like and fulvic-like regions expressing initially the fluorophoric regions of I and II as recorded for HA upon TiO_2 photocatalysis. The most striking intensity was observed in 30 kDa fraction as was also attained for Cu-doped specimens. On the other hand, Cu-doping of TiO_2 specimens did not directly affect the fluorophore intensities excluding any surface interactions due to the substitutional location of Cu species.

Fourier transform infrared and Raman spectroscopy

Under all conditions for all MSFrs, ATR-FTIR and SERS features were evaluated with respect to band positions in a system dependent comparative style.

ATR-FTIR spectroscopic features

Infrared spectra of humic substances have been reported in literature as a complementary tool to identify functional groups within the humic macromolecular arrangements (Davis et al. 1999; Senesi et al. 2003; Sillanpää et al. 2014; Rodríguez et al. 2016). A compilation of the band regions expressed by the aforementioned studies was presented in SI Part 3 Table S1.

It was important to note that a thorough interpretation of infrared spectra of the structural features of humic substances was challenging due to significant overlapping of individual bands by various functional groups (Chen et al. 2002). Although a vast number of researchers investigating FTIR spectra of humic substances mostly utilized powder samples rather than aqueous samples, similar results with different band intensities that were not comparable have been reported in literature. (Summers et al. 1987; Shin et al. 1999; Chen et al. 2002; Rodríguez et al. 2016).

In general, similar ATR-FTIR spectra of the HA MSFrs indicated that chemical structure remained unaltered during the fractionation process. Related findings were reported by investigating the ATR-FTIR spectral features of various lyophilized commercial and standard humic substances composed of humic and fulvic acids (Summers et al. 1987). Shin and colleagues studied the MSFrs of HA by ultrafiltration and indicated that the molecules of the fraction of 100 kDa were primarily aliphatic, while the smaller molecules of 10 kDa fraction were predominantly of aromatic nature (Shin et al. 1999). Rodríguez and co-workers also analyzed various standard and commercial humic/fulvic acids monitoring structural changes by UV–vis and FTIR spectroscopic techniques upon oxidative treatment (Rodríguez et al. 2016).

Detailed ATR-FTIR spectra can be found in SI Part 3. Figure 7 was chosen to be a representative figure and includes the FTIR spectra of all the photocatalysts (TiO_2, synTiO_2, Cu-TiO_2, Cu-synTiO_2) after 60 min of photocatalytic degradation. ATR-FTIR spectra of initial HA and treated HA fractions (initial adsorption, i.e., t = 0 condition, photolysis and photocatalysis) exhibited numerous differences (SI Part 3 Fig. S4-S5). Considering this variation and complexity of the system, ATR-FTIR spectra were presented with respect to specific band comparison rather than based on catalyst-surface explanations. It should be noted that the red and blue shifts in the frequencies of some of the peaks in ATR-FTIR spectra are directly related to the bond lengths of hydrogen bonds where H-bonded complexes can alter either the nature of the shift or the band intensities (Behera and Das 2018). The broad band at 1260–1200 cm^{-1} corresponded to several oxygenated groups, i.e., carboxylic acids, phenols, and aromatic or unsaturated ethers (Kim and Yu 2005; Kim et al. 2006), while some authors attributed it preferentially to C-O stretching and O–H deformation of COOH groups (Chen et al. 2002; Sillanpää et al. 2014). Initial HA spectra showed peaks in this region, which totally disappeared under photolytic conditions as well as through surface attractions resulting in initial adsorption and photocatalysis. Following photocatalysis, notable presence of peaks in lower wavenumber region as 1170–1120 cm^{-1} was assigned to the formation of organic moieties of aliphatic character.

Analysis of ATR-FTIR spectra showed that upon TiO_2 photocatalysis, significant changes in HA MSFrs were detected with the removal of the band at 1455 cm^{-1} that was related with C-H bending, also the bands corresponding to oxygenated groups at ~ 1200 cm^{-1} and the bands at 1095–1030 cm^{-1} that were assigned to C-O stretching. In the presence of synTiO_2, the change was similar, although the band related with C-O stretching of alcohols, and aliphatic ethers was not totally removed. The band centered around 1000–1080 cm^{-1} was observed in all HA MSFrs, however disappeared upon oxidative degradation in all fractions. This band was also related to C-O stretching of alcohols and aliphatic ethers that might either be removed or altered through degradation. Moreover, the emergence of band around 1170–1120 cm^{-1} (C–OH stretching of aliphatic O–H) indicated the formation of organic moieties of aliphatic character following photocatalysis. A new peak around 1337 cm^{-1} emerged upon TiO_2, Cu-TiO_2, and

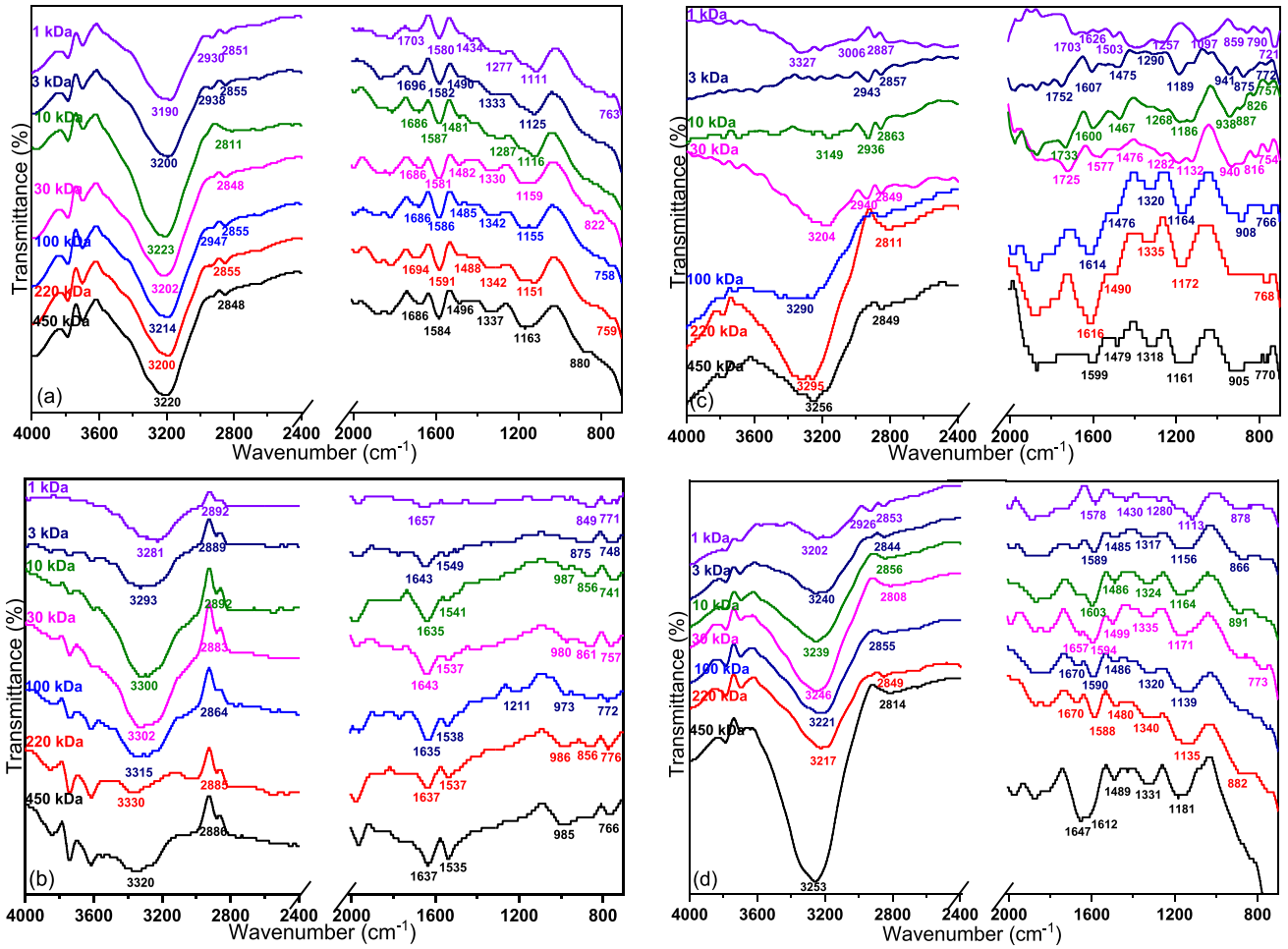

Fig. 7 FTIR spectra of photocatalysts after 60 min photocatalytic degradation. (**a**) TiO_2, (**b**) $synTiO_2$, (**c**) Cu-TiO_2, (**d**) Cu-$synTiO_2$

Cu-$synTiO_2$ photocatalysis that was not evident in initial HA and its MSFrs. The reason could be attributed to NO_3^- formation as reported by Rodríguez and colleagues after ozonation of humic substances (Rodríguez et al. 2016). Data acquired also confirmed NO_2^- (0.0613 mg/L) and NO_3^- (0.1299 mg/L) formation following TiO_2 photocatalysis of HA. As the band around 1460–1440 cm^{-1} corresponded to aliphatic C-H deformation, initial HA showed significant peaks in this band which could not be visualized upon non-oxidative as well as oxidative conditions irrespective of the photocatalyst type. The band at 1630 cm^{-1} was ascribed to either aromatic rings (C = C stretching at about 1650 cm^{-1} was downshifted in conjugated aromatic systems) (Ma 2004) or C = O stretching vibration of double bonds in cyclic and alicyclic compounds, ketones, and quinones (Kim and Yu 2005; Kim et al. 2006) and aromatic carboxylic acids (Lumsdon and Fraser 2005; Pernet-Coudrier et al. 2011). Both features were likely to overlap and contribute together to this band at 1660–1630 cm^{-1} region (Chen et al. 2002; Giovanela et al. 2004). Rodríguez and co-workers reported that this band dropped following ozonation due to preferential ozone attack to aromatic structures (Rodríguez et al. 2016). In a similar fashion, due to non-selective behavior of hydroxyl radical reaction mechanism, the band at 1620–1600 cm^{-1} region either disappeared during photolysis and initial adsorption or decreased in intensity following photocatalysis. The band around 1720 cm^{-1} corresponding to carboxylic groups was not detected in HA spectra upon $synTiO_2$ and Cu-$synTiO_2$ photocatalysis. However, emergence of peaks for MSFrs lower than 30 kDa after Cu-TiO_2 photocatalysis was observed. This might indicate different behavior related to either adsorption on the surface or conversion of carboxylic moieties to CO_2. Hence, analysis of HA spectra recorded upon t = 0 min condition for specified catalysts repetitively showed loss of band at 1720 cm^{-1}; therefore, initial adsorption on the surface was evident under all circumstances (SI Part 3 Fig. S5). Interestingly, only in the presence of Cu-TiO_2, the band at 1660–1630 cm^{-1}

corresponding to C = O stretching of amide groups totally disappeared after photocatalytic oxidation. The peak was apparent in all initial HA MSFrs and respective oxidized fractions upon photocatalysis performed using TiO_2, $synTiO_2$ and $Cu\text{-}TiO_2$. The band around 1260–1200 cm^{-1} that was present in initial HA disappeared totally in the presence of TiO_2 and upshifted to 1267–1241 cm^{-1} band for 450–10 kDa fractions in the presence of $Cu\text{-}synTiO_2$. The band region 1080–1030 cm^{-1} assigned to C-O stretching of polysaccharides or polysaccharide like substances, stretching of alcohols, aliphatic ethers was present in HA however, disappeared by photocatalysis using TiO_2, $synTiO_2$, $Cu\text{-}TiO_2$ and $Cu\text{-}synTiO_2$ and generally upshifted to 1170–1120 cm^{-1} region indicating the evidence of C–OH stretching related to aliphatic O–H. As presented, upon photocatalysis, random changes were observed with respect to photocatalyst type (Fig. 7).

SERS features

As evidenced by infrared spectroscopic features, due to the slight variations in humic structure during photolysis and upon initial surface interactions, application of Raman spectroscopy would not be expected to bring substantial information. Considering that during solar photocatalysis, both the initial as well as the non-adsorbed humic components would concomitantly be present in bulk solution along with the degraded fractions, SERS analyses were selectively performed on initial HA MSFrs and HA subjected to photocatalysis focusing on two key MSFr as 450 kDa and 10 kDa

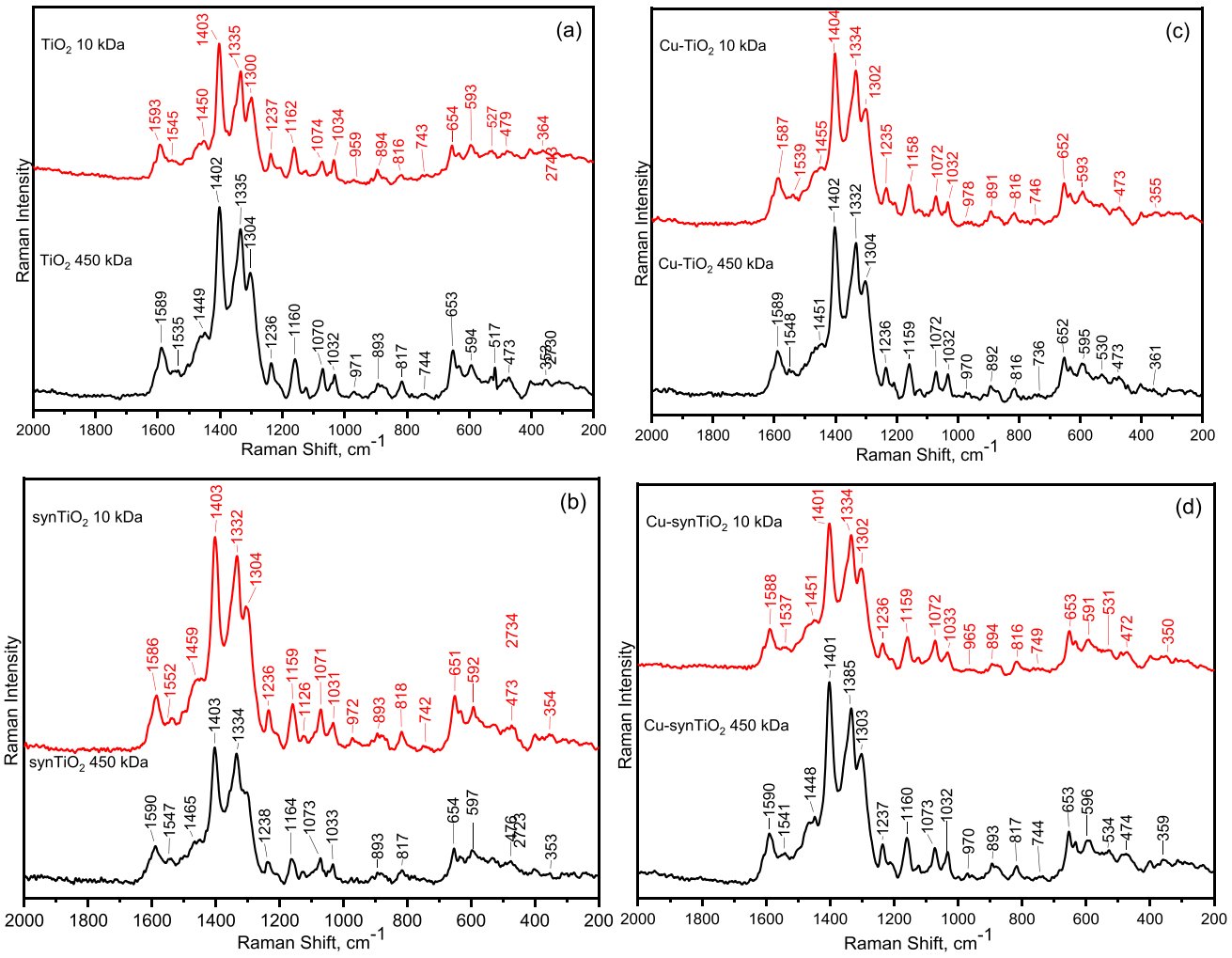

Fig. 8 Fingerprint region of the Raman spectra of HA upon (**a**) TiO_2, (**b**) $synTiO_2$, (**c**) $Cu\text{-}TiO_2$, and (**d**) $Cu\text{-}synTiO_2$ photocatalysis 450 kDa, and 10 kDa

(SI Part 3 Fig. S6-S10). The fingerprint regions of Raman spectra of HA for all photocatalysts were given in Fig. 8.

SERS spectrum of HA 450 kDa size fraction displayed a broad band between 3000 and 2500 cm^{-1} with a maximum at 2730 cm^{-1} as related to asymmetric C-H vibrations corresponding to the aliphatic components. The bands at 1587 cm^{-1} and 1403 cm^{-1} could be attributed to asymmetric and symmetric COO^- vibrations respectively indicating the presence of carboxylate groups (SI Part 3 Table S2). The intense band at 1336 cm^{-1} and a weak band at 1302 cm^{-1} revealed the high aromatic character of HA corresponding to in-plane ring motions of substituted benzene groups. Besides, these bands could be related to the hydroxybenzoic acids and polycyclic aromatic hydrocarbons. A very weak band at 1542 cm^{-1} could be attributed to the ring vibrations of N–H (Francioso et al. 1996; Sánchez-Cortés et al. 1998, 2006). Aromatic ring stretching band at ~ 1600 cm^{-1} was not observed that could be attributed to the possible conformational changes due to the protonation of the carboxylate groups. The result could lead to an enhancement of intramolecular hydrogen bonds and the less orientation of hydrophilic aromatic groups towards the interior of HA matrix (Sánchez-Cortés et al. 1998). The band at 1234 cm^{-1} could be related to C-O stretching motions in phenolic moieties, while the band at 1160 cm^{-1} could be assigned to C-H bending in aromatic rings. The other bands at 1457 cm^{-1} (C-H_2 deformation, C-H bending), 1071 cm^{-1} (C–C stretching, C–OH deformation, C-N stretching), 1030 cm^{-1} (ring breathing vibration C–C aromatic ring stretching (phenylalanine) in proteins), 817 cm^{-1} (C-H out of plane deformation and COO^- deformation), 973 cm^{-1} (aromatic C-H out of plane deformation and anions, SO_3^{2-}), 748 cm^{-1} (out of plane deformation of C-H), 652 cm^{-1} (skeletal ring or C-S stretching and C–C twisting of proteins (tyrosine)), 594 cm^{-1} (C-H out of plane bending), 531 cm^{-1} (out of plane deformation of C–C), and 471 cm^{-1} (C = O out of plane deformation, carbohydrates) could belong to the skeletal vibrations of benzene rings. The band at 354 cm^{-1} as assigned to skeletal rings corresponding to in-plane vibrations of benzene ring coupled with external hydroxyl groups was not noticed. Existence of a wide band at 893 cm^{-1} could be related to the presence of anions. The spectrum of HA 10 kDa MSFr was similar to the high MSFr of HA (450 kDa) expressing the presence of bands with minor downshifts and lower intensities.

From an overall perspective, SERS profiles of humic matter upon TiO_2, synTiO_2, Cu-TiO_2, and Cu-synTiO_2 photocatalysis exhibited strong similarities to spectral characteristics of initial HA (SI Part 3 Fig. S7-S10). Neither the presence of Cu substitutionally located within TiO_2 matrix nor the expected oxidative changes in HA structure affected SERS features (SI Part 3 Fig. S6-S10). A plausible explanation could be attributed to the consecutive removal and formation of main constitutional groups of humic during photocatalysis.

Conclusions

Considering that humic organic matrix is an integrated pool of dissolved compounds with complex interactions, the main purpose of this study was to understand the photocatalytic behavior of different bare and Cu-doped TiO_2 specimens on HA MSFrs.

Photolytic as well as photocatalytic behaviors in the presence of various TiO_2 specimens, i.e., bare TiO_2 (P-25), sol–gel prepared TiO_2 (synTiO_2), and their respective Cu-doped specimens (i.e., Cu-TiO_2 and Cu-synTiO_2) resulted in variations of discrete MSFrs of humic matter upon non-selective/selective degradation mechanism under simulated solar light. Selectivity of different TiO_2 and Cu-doped specimens induced chromophoric changes in humic structure, which could be deduced by specific parameters of UV–vis and fluorescence spectroscopy along with ATR-FTIR and SERS features.

Taking into account high BET surface area and comparatively abundant positive charge of TiO_2 at the reaction pH, steady decrease was observed in all UV vis parameters compared to synTiO_2. Preferential removal of 450 kDa and 220 kDa MSFrs was observed in the presence of TiO_2 relative to synTiO_2. Analysis of specific UV parameters and fluorescence spectral indicators expressed highest values for 450 kDa MSFr and lowest values for 3 kDa fractions of HA. Humic acid molecular size fractions revealed a positive correlation between A_{253}/A_{203} quotient and $CbUV_{254}$ under all conditions covering initial, photolytic, initial adsorption, and photocatalysis expressing an insignificant effect on photocatalyst type. In general, $FI_{sync470}$ parameter of MSFrs pointed out the possible degradation pathways proceeding either on the surface of the photocatalyst or in close vicinity of the surface.

Upon photolysis, FI values of all HA MSFrs displayed insignificant variations. However, by initial adsorption, all MSFrs excluding 1 kDa fraction displayed almost similar FI values through a stepwise increase as "450 kDa-220 kDa," "100 kDa-10 kDa," and a steep increase. On the other hand, all photocatalyst specimens expressed almost similar tendencies with minor changes for Cu-TiO_2 most probably due to the presence of substitutional Cu onTiO_2 surface. Cu doping could only induce intra-system diversity in degradation pathway affecting the performance of the photocatalyst specimen rather than bringing significant alteration in HA structure.

Excluding non-specific effect of photolysis, system-dependent minor variations were deduced by Raman and SERS data. Complex and diverse organic associations of

humic matter MSFrs were reflected in all spectral features although organic carbon pool was subjected to photocatalytic degradation and thereby to incomplete mineralization. All spectroscopic parameters demonstrated inconsequential role of Cu-doping enabling the utilization of solar light.

Supplementary Information The online version contains supplementary material available at https://doi.org/10.1007/s11356-022-21754-1.

Author contribution Miray Bekbolet, Nazli Turkten, and Ceyda S. Uyguner-Demirel contributed to the study conception and design. Material preparation, data collection, and analysis were performed by Nazli Turkten, Dila Kaya, Ceyda S. Uyguner-Demirel, and Miray Bekbolet. All authors contributed, read, and approved the final version of the manuscript.

Data availability Not applicable.

Declarations

Ethics approval Not applicable.

Consent to participate Not applicable.

Consent for publication Not applicable.

Competing interests The authors declare no competing interests.

References

Badawi A, Althobaiti MG (2021) Effect of Cu-doping on the structure, FT-IR and optical properties of titania for environmental-friendly applications. Ceram Int 47:11777–11785. https://doi.org/10.1016/j.ceramint.2021.01.018

Baker A, Tipping E, Thacker SA, Gondar D (2008) Relating dissolved organic matter fluorescence and functional properties. Chemosphere 73:1765–1772. https://doi.org/10.1016/j.chemosphere.2008.09.018

Behera B, Das PK (2018) Blue-and red-shifting hydrogen bonding: a gas phase FTIR and Ab initio study of RR′ CO··· $DCCl_3$ and RR′ S··· $DCCl_3$ complexes. J Phys Chem A 122:4481–4489. https://doi.org/10.1021/acs.jpca.7b11962

Bekbolet M, Sen Kavurmaci S (2015) The effect of photocatalytic oxidation on molecular size distribution profiles of humic acid. Photochem Photobiol Sci 14:576–582. https://doi.org/10.1039/c4pp00262h

Boccuzzi F, Chiorino A, Martra G, Gargano M, Ravasio N, Carrozzini B (1997) Preparation, characterization, and activity of Cu/TiO_2 catalysts. I. Influence of the preparation method on the dispersion of copper in Cu/TiO_2. J Catal 165:129–139. https://doi.org/10.1006/jcat.1997.1475

Bokhimi X, Morales A, Novaro O, López T, Chimal O, Asomoza M, Gómez R (1997) Effect of copper precursor on the stabilization of titania phases, and the optical properties of Cu/TiO_2 prepared with the sol-gel technique. Chem Mater 9:2616–2620. https://doi.org/10.1021/cm970279r

Brezinski K, Gorczyca B (2019) Multi-spectral characterization of natural organic matter (NOM) from Manitoba surface waters using high performance size exclusion chromatography (HPSEC). Chemosphere 225:53–64. https://doi.org/10.1016/j.chemosphere.2019.02.176

Capasso S, Chianese S, Musmarra D, Iovino P (2020) Macromolecular structure of a commercial humic acid sample. Environments 7:32. https://doi.org/10.3390/environments7040032

Chen W, Yu H-Q (2021) Advances in the characterization and monitoring of natural organic matter using spectroscopic approaches. Water Res 190:116759. https://doi.org/10.1016/j.watres.2020.116759

Chen J, Gu B, LeBoeuf E, Pan H, Dai S (2002) Spectroscopic characterization of the structural and functional properties of natural organic matter fractions. Chemosphere 48:59–68. https://doi.org/10.1016/S0045-6535(02)00041-3

Chi F-H, Amy GL (2004) Kinetic study on the sorption of dissolved natural organic matter onto different aquifer materials: the effects of hydrophobicity and functional groups. J Colloid Interface Sci 274:380–391. https://doi.org/10.1016/j.jcis.2003.12.049

Chin Y-P, Aiken G, O'Loughlin E (1994) Molecular weight, polydispersity, and spectroscopic properties of aquatic humic substances. Environ Sci Technol 28:1853–1858. https://doi.org/10.1021/es00060a015

Coble PG (1996) Characterization of marine and terrestrial DOM in seawater using excitation-emission matrix spectroscopy. Mar Chem 51:325–346. https://doi.org/10.1016/0304-4203(95)00062-3

Coloma F, Marquez F, Rochester CH, Anderson CA (2000) Determination of the nature and reactivity of copper sites in Cu-TiO_2 catalysts. Phys Chem Chem Phys 2:5320–5327. https://doi.org/10.1039/b005331g

Colón G, Maicu M, Hidalgo MC, Navío J.A. (2006) Cu-doped TiO_2 systems with improved photocatalytic activity. Applied Catalysis B: Environmental 67(1–2):41–51. https://doi.org/10.1016/j.apcatb.2006.03.019

Dalrymple RM, Carfagno AK, Sharpless CM (2010) Correlations between dissolved organic matter optical properties and quantum yields of singlet oxygen and hydrogen peroxide. Environ Sci Technol 44:5824–5829. https://doi.org/10.1021/es101005u

Davis WM, Erickson CL, Johnston CT, Delfino JJ, Porter JE (1999) Quantitative Fourier transform infrared spectroscopic investigation of humic substance functional group composition. Chemosphere 38:2913–2928. https://doi.org/10.1016/S0045-6535(98)00486-X

Del Vecchio R, Blough NV (2004) On the origin of the optical properties of humic substances. Environ Sci Technol 38:3885–3891. https://doi.org/10.1021/es049912h

Edzwald JK, Becker WC, Wattier KL (1985) Surrogate parameters for monitoring organic matter and THM precursors. J AWWA 77:122–132. https://doi.org/10.1002/j.1551-8833.1985.tb05521.x

Emeline AV, Ryabchuk V, Serpone N (2000) Factors affecting the efficiency of a photocatalyzed process in aqueous metal-oxide dispersions Prospect of distinguishing between two kinetic models. J Photochem Photobiol a: Chem 133:89–97. https://doi.org/10.1016/S1010-6030(00)00225-2

Francioso O, Sanchez-Cortes S, Tugnoli V, Ciavatta C, Sitti L, Gessa C (1996) Infrared, Raman, and nuclear magnetic resonance (^{1}H, ^{13}C, and ^{31}P) spectroscopy in the study of fractions of peat humic acids. Appl Spectrosc 50:1165–1174. https://doi.org/10.1366/0003702963905169

Ganesh I, Kumar PP, Annapoorna I, Sumliner JM, Ramakrishna M, Hebalkar NY, Padmanabham G, Sundararajan G (2014) Preparation and characterization of Cu-doped TiO_2 materials for electrochemical, photoelectrochemical, and photocatalytic applications. Appl Surf Sci 293:229–247. https://doi.org/10.1016/j.apsusc.2013.12.140

Giovanela M, Parlanti E, Soriano-Sierra J, Soldi MS, Sierra MMD (2004) Elemental compositions, FT-IR spectra and thermal behavior of sedimentary fulvic and humic acids from aquatic and terrestrial environments. Geochem J 38:255–264. https://doi.org/10.2343/geochemj.38.255

Gowland DCA, Robertson N, Chatzisymeon E (2021) Photocatalytic oxidation of natural organic matter in water. Water 13:288. https://doi.org/10.3390/w13030288

Hatchard CG, Parker CA (1956) A new sensitive chemical actinometer-II. Potassium ferrioxalate as a standard chemical actinometer. Proc R Soc Lond A 235:518–536. https://doi.org/10.1098/rspa.1956.0102

Hansen AM, Kraus TE, Pellerin BA, Fleck JA, Downing BD, Bergamaschi BA (2016) Optical properties of dissolved organic matter (DOM): Effects of biological and photolytic degradation. Limnol Oceanogr 61:1015–1032. https://doi.org/10.1002/lno.10270

Hayes MHB, MacCarthy P, Malcolm RL, Swift RS (1989) Humic Substances II. In Search of Structure. John Wiley & Sons Ltd., Chichester, UK

Her N, Amy G, Chung J, Yoon J, Yoon Y (2008) Characterizing dissolved organic matter and evaluating associated nanofiltration membrane fouling. Chemosphere 70:495–502. https://doi.org/10.1016/j.chemosphere.2007.06.025

Hua L-C, Chao S-J, Huang K, Huang C (2020) Characteristics of low and high SUVA precursors: relationships among molecular weight, fluorescence, and chemical composition with DBP formation. Sci Total Environ 727:138638. https://doi.org/10.1016/j.scitotenv.2020.138638

Hur J, Schlautman MA (2003) Molecular weight fractionation of humic substances by adsorption onto minerals. J Colloid Interface Sci 264:313–321. https://doi.org/10.1016/S0021-9797(03)00444-2

Johnson WP, Bao G, John WW (2002) Specific UV absorbance of Aldrich Humic Acid: changes during transport in aquifer sediment. Environ Sci Technol 36:608–616. https://doi.org/10.1021/es010920x

Kerrami A, Khezami L, Bououdina M, Mahtout L, Modwi A, Rabhi S, Bensouici F, Belkacemi H (2021) Efficient photodegradation of azucryl red by copper-doped TiO_2 nanoparticles—experimental and modeling studies. Environ Sci Technol 28:57543–57556. https://doi.org/10.1007/s11356-021-14682-z

Kerc A, Bekbolet M, Saatci AM (2004) Effects of oxidative treatment techniques on molecular size distribution of humic acids. Water Sci Technol 49:7–12. https://doi.org/10.2166/wst.2004.0205

Kim HC, Yu MJ (2005) Characterization of natural organic matter in conventional water treatment processes for selection of treatment processes focused on DBPs control. Water Res 39:4779–4789. https://doi.org/10.1016/j.watres.2005.09.021

Kim HC, Yu MJ, Han I (2006) Multi-method study of the characteristic chemical nature of aquatic humic substances isolated from the Han River, Korea. Appl Geochem 21:1226–1239. https://doi.org/10.1016/j.apgeochem.2006.03.011

Korak JA, Dotson AD, Summers RS, Rosario-Ortiz FL (2014) Critical analysis of commonly used fluorescence metrics to characterize dissolved organic matter. Water Res 49:327–338. https://doi.org/10.1016/j.watres.2013.11.025

Korshin GV, Li C-W, Benjamin MM (1997) Monitoring the properties of natural organic matter though UV spectroscopy: a consistent theory. Water Res 31:1787–1795. https://doi.org/10.1016/S0043-1354(97)00006-7

Kumar SG, Devi LG (2011) Review on modified TiO_2 photocatalysis under UV/Visible light: selected results and related mechanisms on interfacial charge carrier transfer dynamics. J Phys Chem A 115:13211–13241. https://doi.org/10.1021/jp204364a

Langhals H, Abbt-Braun G, Frimmel FH (2000) Association of humic substances: verification of Lambert-Beer Law. Acta Hydrochim Hydrobiol 28:329–332. https://doi.org/10.1002/1521-401X(200012)28:6%3c329::AID-AHEH329%3e3.0.CO;2-E

Lee PC, Meisel D (1982) Adsorption and surface-enhanced Raman of dyes on silver and gold sols. J Phys Chem 86:3391–3395. https://doi.org/10.1021/j100214a025

Li Y, Niu J, Shang E, Crittenden JC (2016) Influence of dissolved organic matter on photogenerated reactive oxygen species and metal-oxide nanoparticle toxicity. Water Res 98:9–18. https://doi.org/10.1016/j.watres.2016.03.050

Loiselle A, Vione D, Minero C, Maurino V, Tognazzi A, Dattilo AM, Rossi C, Bracchini L (2012) Chemical and optical phototransformation of dissolved organic matter. Water Res 46:3197–3207. https://doi.org/10.1016/j.watres.2012.02.047

Lumsdon DG, Fraser AR (2005) Infrared spectroscopic evidence supporting heterogeneous site binding models for humic substances. Environ Sci Technol 39:6624–6631. https://doi.org/10.1021/es050180i

Ma YS (2004) Reaction mechanisms for DBPs reduction in humic acid ozonation. Ozone Sci Eng 26:153–164. https://doi.org/10.1080/01919510490439429

Moretti E, Cattaruzza E, Flora C, Talon A, Casini E, Vomiero A (2021) Photocatalytic performance of Cu-doped titania thin films under UV light irradiation. Appl Surf Sci 553:149535. https://doi.org/10.1016/j.apsusc.2021.149535

Noman MT, Ashraf MA, Ali A (2019) Synthesis and applications of nano-TiO_2: a review. Environ Sci Pollut Res 26:3262–3291. https://doi.org/10.1007/s11356-018-3884-z

Navarro-Pedreño J, Almendro-Candel MB, Zorpas AA (2021) The increase of soil organic matter reduces global warming, Myth or Reality? Sci 3:18. https://doi.org/10.3390/sci3010018

Parilti NB, Uyguner-Demirel CS, Bekbolet M (2011) Response surface methodological approach for the assessment of the photocatalytic degradation of NOM. J Photochem Photobiol a: Chem 225:26–35. https://doi.org/10.1016/j.jphotochem.2011.09.021

Pernet-Coudrier B, Varrault G, Saad M, Croué JP, Dignac MF, Mouchel JM (2011) Characteristics of dissolved organic matter in Parisian urban aquatic systems: predominance of hydrophilic and proteinaceous structures. Biogeochemistry 106:89–106. https://doi.org/10.1007/s10533-010-9480-z

Pitois A, Abrahamsen LG, Ivanov PI, Bryan DB (2008) Humic acid sorption onto a quartz sand surface: a kinetic study and insight into fractionation. J Colloid Interface Sci 325:93–100. https://doi.org/10.1016/j.jcis.2008.05.031

Porcal P, Koprivnjak J-F, Molot LA, Dillon PJ (2009) Humic substances-Part 7: The biogeochemistry of dissolved organic carbon and its interactions with climate change. Environ Sci Pollut Res 16:714–726. https://doi.org/10.1007/s11356-009-0176-7

Rodríguez FJ, Schlenger P, García-Valverde M (2014a) A comprehensive structural evaluation of humic substances using several fluorescence techniques before and after ozonation. Part I: Structural characterization of humic substances. Sci Total Environ 476–477:718–730. https://doi.org/10.1016/j.scitotenv.2013.11.150

Rodríguez FJ, Schlenger P, García-Valverde M (2014b) A comprehensive structural evaluation of humic substances using several fluorescence techniques before and after ozonation. Part II: Evaluation of structural changes following ozonation. Sci Total Environ 476–477:731–742. https://doi.org/10.1016/j.scitotenv.2013.11.149

Rodríguez FJ, Schlenger P, García-Valverde M (2016) Monitoring changes in the structure and properties of humic substances following ozonation using UV-Vis, FTIR and ^{1}H NMR techniques. Sci Total Environ 541:623–637. https://doi.org/10.1016/j.scitotenv.2015.09.127

Sánchez-Cortés S, Corrado G, Trubetskaya OE, Trubetskoj OA, Hermosin B, Saiz-Jimenez C (2006) Surface-enhanced Raman spectroscopy of Chernozem humic acid and their fractions obtained by coupled size exclusion chromatography-Polyacrylamide gel

electrophoresis (SEC-PAGE). Appl Spectrosc 60:48–53. https://doi.org/10.1366/000370206775382695

Sánchez-Cortés S, Francioso O, Ciavatta C, García-Ramos JV, Gessa C (1998) pH-dependent adsorption of fractionated peat humic substances on different silver colloids studied by surface-enhanced Raman spectroscopy. J Colloid Interface Sci 198:308–318. https://doi.org/10.1006/jcis.1997.5293

Scott AI (1964) Interpretation of the Ultraviolet Spectra of Natural Products. Pergamon Press, New York,. https://doi.org/10.1016/C2013-0-02266-9

Senesi N, D'Orazio V, Ricca G (2003) Humic acids in the first generation of EUROSOILS. Geoderma 116(3–4):325–344. https://doi.org/10.1016/S0016-7061(03)00107-1

Shin H-S, Monsallier JM, Choppin GR (1999) Spectroscopic and chemical characterizations of molecular size fractionated humic acid. Talanta 50:641–647. https://doi.org/10.1016/S0039-9140(99)00161-7

Sillanpää M, Matilainen A, Lahtinen T (2014) Characterization of NOM in natural organic matter in water. Sillanpää M Characterization and Treatment Methods, 1st edn. IWA publishing, Elsevier, London, pp 17–53

Summers RS, Cornel PK, Roberts PV (1987) Molecular size distribution and spectroscopic characterization of humic substances. Sci Total Environ 62:27–37. https://doi.org/10.1016/0048-9697(87)90478-5

Tanaka T (2012) Functional groups and reactivity of size-fractionated Aldrich humic acid. Thermochim Acta 532:60–64. https://doi.org/10.1016/j.tca.2011.12.004

Thomson J, Parkinson A, Roddick FA (2004) Depolymerization of chromophoric natural organic matter. Environ Sci Technol 38:3360–3369. https://doi.org/10.1021/es049604j

Tian W, Yang Z, Zhang X, Ma W, Jiang J (2018) Redox properties of humic substances under different environmental conditions. Environ Sci Pollut Res 25:25734–25743. https://doi.org/10.1007/s11356-017-9506-3

Turkten N, Bekbolet M (2020) Photocatalytic performance of titanium dioxide and zinc oxide binary system on degradation of humic matter. J Photochem Photobiol a: Chem 401:112748. https://doi.org/10.1016/j.jphotochem.2020.112748

Turkten N, Cinar Z, Tomruk A, Bekbolet M (2019) Copper doped TiO_2 photocatalysts: application to drinking water by humic matter degradation. Environ Sci Pollut Res 26:36096–36106. https://doi.org/10.1007/s11356-019-04474-x

Uyguner CS, Bekbolet M (2005) Implementation of spectroscopic parameters for practical monitoring of natural organic matter. Desalination 176:47–55. https://doi.org/10.1016/j.desal.2004.10.027

Uyguner CS, Bekbolet M (2007) A review on the photocatalytic degradation of humic substances. In: Nikolau A, Selçuk H, Rizzo L (eds) Control of Disinfection By-Products in Drinking Water Systems, 1st edn. NOVA Science Publishers Inc., New York-USA, pp 419–446

Uyguner CS, Bekbolet M (2009) Application of photocatalysis for the removal of natural organic matter in simulated surface and ground waters. J Adv Oxid Technol 12:87–92. https://doi.org/10.1515/jaots-2009-0110

Uyguner-Demirel CS, Bekbolet M (2011) Significance of analytical parameters for the understanding of natural organic matter in relation to photocatalytic oxidation. Chemosphere 84:1009–1031. https://doi.org/10.1016/j.chemosphere.2011.05.003

Uyguner-Demirel CS, Birben NC, Bekbolet M (2017) Elucidation of background organic matter matrix effect on photocatalytic treatment of contaminants using TiO_2: a review. Catal Today 284:202–214. https://doi.org/10.1016/j.cattod.2016.12.030

Uyguner-Demirel CS, Birben NC, Bekbolet M (2018) A comprehensive review on the use of second generation TiO_2 photocatalysts: microorganism inactivation. Chemosphere 211:420–448. https://doi.org/10.1016/j.chemosphere.2018.07.121

Wu Q-Y, Zhou T-H, Du Y, Ye B, Wang W-L, Hu H-Y (2020) Characterizing the molecular weight distribution of dissolved organic matter by measuring the contents of electron-donating moieties, UV absorbance, and fluorescence intensity. Environ Int 137:105570. https://doi.org/10.1016/j.envint.2020.105570

Yalçın Y, Kılıç M, Çınar Z (2010) Fe^{3+}-doped TiO_2: A combined experimental and computational approach to the evaluation of visible light activity. Appl Catal B 99:469–477. https://doi.org/10.1016/j.apcatb.2010.05.013

Yang X-J, Wang S, Sun H-M, Wang X-B, Lian J-S (2015) Preparation and photocatalytic performance of Cu-doped TiO_2 nanoparticles. Trans Nonferrous Met Soc China 25:504–509. https://doi.org/10.1016/S1003-6326(15)63631-7

Yu J, Kiwi J, Wang T, Pulgarin C, Rtimi S (2019) Evidence for a dual mechanism in the TiO_2/CuxO photocatalyst during the degradation of sulfamethazine under solar or visible light: Critical issues. J Photochem Photobiol a: Chem 375:270–279. https://doi.org/10.1016/j.jphotochem.2019.02.033

Zhang M, Sun R, Li Y, Shi Q, Xie L, Chen J, Xu X, Shi H, Zhao W (2016) High H_2 evolution from quantum Cu(II) nanodot-dopedtwo-dimensional ultrathin TiO_2 nanosheets with dominant exposed {001} facets for reforming glycerol with multipleelectron transport pathways. The Journal of Physical Chemistry C 120(20):10746–10756. https://doi.org/10.1021/acs.jpcc.6b01030

Zhang S, Hao Z, Liu J, Gutierrez L, Croúe J-P (2021) Molecular insights into the reactivity of aquatic natural organic matter towards hydroxyl (•OH) and sulfate ($SO_4^{\bullet-}$) radicals using FT-ICR MS. Chem Eng J 425:130622. https://doi.org/10.1016/j.cej.2021.130622